**US Army Corps
of Engineers**®
Engineer Research and
Development Center

Material Specifications for Attack Countermeasures on Bridges

Advanced Cementitious Materials for Blast Protection

Andrew B. Groeneveld and C. Kennan Crane   April 2023

Advanced Cementitious Materials for Blast Protection

Andrew B. Groeneveld and C. Kennan Crane

Geotechnical and Structures Laboratory
US Army Engineer Research and Development Center
3909 Halls Ferry Road
Vicksburg, MS 39180-6199

Final report

Abstract

Advanced cementitious materials, commonly referred to as ultra-high performance concretes (UHPCs), are developing rapidly and show promise for civil infrastructure and protective construction applications. Structures exposed to blasts experience strain rates on the order of 10^2 s^{-1} or more. While a great deal of research has been published on the durability and the static properties of UHPC, there is less information on its dynamic properties. The purpose of this report is to (1) compile existing dynamic property data—including compressive strength, tensile strength, elastic modulus, and energy absorption—for six proprietary and research UHPCs and (2) implement a single-degree-of-freedom (SDOF) model for axisymmetric UHPC panels under blast loading as a means of comparing the UHPCs. Although simplified, the model allows identification of key material properties and promising materials for physical testing. Model results indicate that tensile strength has the greatest effect on panel deflection, with unit weight and elastic modulus having a moderate effect. CEMTEC$_{multiscale}$® deflected least in the simulation. Lafarge Ductal®, a commonly available UHPC in North America, performed in the middle of the five UHPCs considered.

Contents

Report Documentation Page

Figures and Tables

Figures

Tables

Preface

This study was conducted for the Federal Highway Administration under IAA DTFH61-13-X-30049, "Material Specifications for Attack Countermeasures on Bridges." The technical monitor was Mr. Eric Munley.

The work was performed between May and August 2014 by the Structural Engineering Branch (GSS) of the Geosciences and Structures Division (GS), US Army Engineer Research and Development Center, Geotechnical and Structures Laboratory (ERDC-GSL). At the time of publication, Ms. Mariely Mejias-Santiago was chief, GSS; and Mr. James L. Davis was chief, GS. The deputy director of ERDC-GSL was Mr. Charles W. Ertle II, and the director was Mr. Bartley P. Durst.

COL Christian Patterson was the commander of ERDC, and Dr. David W. Pittman was the director.

1 Introduction

1.1 Background

This report summarizes the relevant high-strain-rate properties of several advanced cementitious materials in the open literature and uses those properties in a single-degree-of-freedom (SDOF) model for approximate analysis of panels under blast loads. These materials are commonly, if not entirely accurately, referred to as ultra-high performance concretes (UHPCs). UHPC is defined by American Concrete Institute Committee 239 as having "a minimum specified compressive strength of 22,000 psi[1] (150 MPa) with specified durability[,] tensile ductility[,] and toughness requirements; fibers are generally included to achieve specified requirements" (ACI 2018). Strain rates in materials subjected to a blast event are typically in the range of 10^2 to 10^4 s^{-1} (Ngo et al. 2007a). If the properties of materials used in blast protection exhibit strain rate effects, then the dynamic properties are vital for designing blast protection systems for bridges and other structures. The dynamic properties of these materials are not extremely well-understood, and there is even some dispute if the strain-rate sensitivity of UHPC is greater than or less than that of normal strength concrete (NSC). Work by Habel and Gauvreau (2008) and Parant et al. (2007) posit that UHPC is more rate sensitive, while results from works such as Solomos and Berra (2004), Rong et al. (2010), and Lai and Sun (2009) suggest that sensitivity decreases with increasing strength.

1.2 Approach

Because the dynamic properties of the various UHPCs are not completely characterized, the data presented in this report are necessarily incomplete. Also, the properties that have been characterized and the extent of the study vary widely between materials. This variability makes meaningful comparisons and conclusions more difficult. The aim here is to provide enough information to make preliminary judgments about promising materials and to inform decision making for subsequent experimental study. One last caveat, raised by Banthia (2005), relates to comparing dynamic properties between studies. There are many effects that are difficult to account for: energy dissipation in machines,

---

[1] For a full list of the spelled-out forms of the units of measure used in this document, please refer to *US Government Publishing Office Style Manual*, 31st ed. (Washington, DC: US Government Publishing Office, 2016), 248–252, https://www.govinfo.gov/content/pkg/GPO-STYLEMANUAL-2016/pdf/GPO-STYLEMANUAL-2016.pdf.

specimen size and geometry, consideration (or neglect) of inertial loading, and the lack of standardized test methods.

Once candidate materials for blast protection are identified, the SDOF model can be used for preliminary comparison of the materials under blast loading without the cost of physical testing. An advantage of SDOF models is their simplicity and rapid generation of results. SDOF models are also useful when the variables (material properties, loads, etc.) are not known with precision but results are needed for member sizing or approximate sensitivity studies. The materials likely to incur the least damage under a given blast loading can then be selected for physical testing at a future date to verify results. Also, a regression analysis of the results can identify apparent correlations between material properties and the maximum deflection under blast loading.

The panel is modeled using Kirchhoff plate theory, and the words *panel* and *plate* are used interchangeably in this report. Only bending effects are considered. Material resistance is modeled as elastic-plastic, with partial failure determined using the Mohr-Coulomb criterion. Equivalent properties were calculated so the real panel is approximated by a mass-spring system in the SDOF model. The equation of motion for the mass-spring system was solved using two different numerical integration methods to compare results.

1.3 Objective

This work is divided into two phases–a literature review and an SDOF model–with the objectives for each phase defined as follows. The objectives for the literature review are to provide enough information to make preliminary judgments about promising materials and to inform decision-making for subsequent experimental study. The objective for the SDOF model is to enable preliminary comparison of the materials under blast loading without the cost of physical testing.

2   Materials

The primary focus was on commercially available UHPCs and reasonably well-established academic UHPCs. Ductal®, produced by Lafarge North America, is the most readily available commercial UHPC in North America. Densit®, produced by Densit ApS (Denmark), although difficult to obtain in the United States, was still considered because of its use in security applications. Other commercial UHPCs not considered were BCV® (Béton Composite Vicat), produced by Vicat (France); Ceracem®, produced by Béton Spécial Industriel (France); and CRC® (Compact Reinforced Concrete), produced by CRC Technology (Denmark). Reasons for exclusion include a lack of dynamic properties data and limited or no availability on the US market.

The US Army Corps of Engineers (USACE) has developed a UHPC called Cor-Tuf at the Engineer Research and Development Center (ERDC) (Williams et al. 2009). However, Cor-Tuf was not considered in this study due to distribution limitations on some of the Cor-Tuf literature.

As shown by Graybeal (2006), the curing regime has a large effect on the properties of hardened UHPC. Thus, in this report, when data are presented from a study, the method of curing is also noted whenever possible. For some studies, information on curing regime is incomplete or missing.

2.1   Ductal®

Lafarge has six main Ductal® products available on the US market, as listed in Table 1. The static compressive strength f'_{cs} is given merely as a relative measure of the different products' strengths. Many other material properties come into play in blast loading, especially dynamic properties, which are the focus of this report and will be dealt with in detail in the following sections. Of the six listed products, BS1000 and CS1000 are the most promising for use in blast protection, as they have the highest strengths (compressive, flexural, and tensile) and stiffnesses (Lafarge Canada Inc. 2009a; Lafarge Canada Inc. 2009b). In a recent study by Ellis et al. (2014), Ductal® BS1000 was used to cast panels for blast-load testing at ERDC. However, specifics on the Ductal® mix used are often absent in many works.

Table 1. Lafarge Ductal® product family (Lafarge 2014).

Product	Intended Use	Mean Static f'_{cs} (ksi)	Applications
AN1000	Architectural	17	Facades, canopies, and louvers
AR1000	Architectural	15	Decoration (interior and exterior)
BS1000	Structural	26	Columns, long span roofs/floors, seismic elements, wall panels, and modular precast systems
CS1000	Structural	26	Bridges, decks, marine docks/walls, troughs, piles, and leave-in-place forms
JS1000	Structural	20	Field casting of joints for precast deck panel bridges
JS1100RS	Structural	20	Rapid-setting version of JS1000, attains design strength within roughly 48 hr

Refer to Graybeal (2006) for information on the composition of Ductal® or to Zdeb (2013) for additional background on reactive powder concrete (RPC), on which Ductal® is based.

2.2 Densit®

Of the many cement and concrete products produced by Densit ApS, the four listed in Table 2 were given preliminary consideration for use in blast protection. These products are mainly marketed to the energy and security industries. Again, the static compressive strength f'_{cs} is given merely as a relative measure of the different products' strengths. Many other material properties come into play in blast loading and are the focus of this report.

Table 2. Selected products in the Densit® family (Densit ApS, "Ducorit"; Densit ApS, "Flexbinder"; Densit ApS, "Inducast").

Product	Intended Use	Mean Static f'_{cs} (ksi)	Applications
Ducorit® D4	Structural	29	Grouted connections in wind turbine foundations and oil and gas rigs
Ducorit® S5	Structural	18	Grouted connections
Flexbinder	Security	34	Casting of ATMs
Inducast TT5	Security	43	Construction of lightweight, break-in-resistant elements

Despite the promising mechanical performance exhibited by Inducast TT5, no test information other than the manufacturer's data sheet (Densit ApS, "Inducast") exists in the literature. Therefore, this investigation was limited to Ducorit® D4, Ducorit® S5, and Flexbinder. However, Inducast TT5 still warrants attention for blast protection, especially for dynamic properties testing.

2.3 B4Q/B5Q

The University of Kassel, Germany, has performed in-depth research on the development of UHPC mix designs (Fehling et al. 2005). The B4Q and B5Q mixes incorporate basalt and quartz aggregates as well as steel-fiber reinforcement. The steel fibers used are 0.059 in. in diameter by 0.35 in. in length. Mix designs for the three mixes examined herein are shown in Table 3. The mixes are denoted B4Q/0, B4Q/1.0, and B5Q/2.5, with the number after the solidus (/) indicating the volume percentage of steel fibers.

Table 3. B4Q and B5Q mix designs (Fehling et al. 2005; Thoma et al. 2012).

Components	Weight (lb/yd³)		
	B4Q/0	B4Q/1.0	B5Q/2.5
Steel fiber content (vol %)	0	1.0	2.5
Cement (CEM I 52.5 R HS NA)	1123	1113	1096
Water	273	273	266
Basalt, split (max. diameter 8 mm)	1022	1032	1007
Quartz sand (max. diameter 0.5 mm)	612	612	597
Fine quartz	787	781	769
Silica fume	305	303	298
Superplasticizer	38.8	51.3	50.6
Steel fibers (ø 0.15 x 9 mm)	0	132	327

2.4 UHPC-based composite

Researchers at Nanjing University and Southeast University, Nanjing, China, have developed what they term "UHPC-based composites," or UHPCCs (Rong et al. 2010; Lai and Sun 2008; Lai and Sun 2009; Lai and Sun 2010). These mixes incorporate a significant amount of fly ash and blast furnace slag for greater economy. Mix designs for the six formulations examined in this work are shown in Table 4.

Table 4. UHPCC mix designs (Rong et al. 2010; Lai and Sun 2008).

Components	Weight (lb/yd³)					
	Without coarse aggregate			With coarse aggregate		
Steel fiber content (vol %)	0	3	4	0	2	3
Cement (P-II Grade 52.5)	674	674	674	674	674	674
Silica fume	169	169	169	169	169	169
Ultra-fine fly ash	422	422	422	422	422	422
Ultra-fine slag	422	422	422	422	422	422
Sand (max. diameter 2.5 mm)	2023	2023	2023	2023	2023	2023
Basalt (max. diameter 10 mm)	0	0	0	2023	2023	2023
Superplasticizer (polycarboxylic HRWR)	33.7	33.7	33.7	33.7	33.7	33.7
Water	253	270	270	270	287	287

2.5 Multiscale fiber-reinforced concrete

The primary multiscale fiber-reinforced concrete (MSFRC) researched was CEMTEC_multiscale®, developed by the Laboratoire Central des Ponts et Chaussées (LCPC) in Paris. As the name suggests, the mix incorporates multiple sizes of steel fibers. Three fiber lengths are used: (1) less than 0.08 in., (2) between 0.08 and 0.28 in., and (3) greater than or equal to 0.79 in. The details on fiber geometry are trade secrets. Total fiber content is equivalent to 11% by volume. The mix design is shown in Table 5.

Table 5. CEMTEC_multiscale® mix design (Rossi and Parant 2008).

Components	Weight (lb/yd³)
Cement (CPA CEMI 52.5 R)	1770
Sand (Quartz 125-400 µm)	867
Silica fume (from zirconium industry)	452
Superplasticizer (Polyphosphonate - 30%)	74
Water	356
Total steel fibers	1512

An overview of several MSFRCs is given in Park et al. (2012); other MSFRCs include ultra-high performance fiber-reinforced concrete (Millard et al. 2010), and CARDIFRC® (Karihaloo 2012). Unfortunately, little information on dynamic properties is available for most MSFRCs.

2.6 Engineered cementitious composite

Engineered cementitious composite (ECC) was designed based on a micromechanical design philosophy (Li 2003). While not technically classified as a UHPC, ECC performs well in tension, with a tensile strain capacity of up to 5% (Li et al. 2001). The mix proportions of four selected ECCs are given in Table 6. Additional information on the type of fibers added and the admixtures used can be found in the references for the mixes.

Douglas and Billington (2005) used short, high-modulus polyvinyl alcohol (PVA) fibers in their mix, herein referred to as PVA-ECC. In creating their lightweight ECC (LW-ECC), Wang and Li (2003) used REC15 PVA fibers (Kuralon K-II REC15, supplied by Kuraray Co. Ltd.), which are 0.47 in. long but only 0.0015 in. in diameter. The fibers have a tensile strength of 158 ksi and an elastic modulus of 6206 ksi. Maalej et al. (2005) created a hybrid fiber ECC (HF-ECC) that could also be classified as an MSFRC. Two types of fibers were used: (1) steel fibers 0.51 in. long and 0.0063 in. in diameter with an elastic modulus of 29000 ksi and a tensile strength of 362 ksi and (2) polyethylene (PE) fibers 0.47 in. long and 0.0015 in. in diameter with an elastic modulus of 9570 ksi and a tensile strength of 378 ksi. Mechtcherine et al. (2011) termed their ECC a strain-hardening cement-based composite (SHCC). These researchers also used the REC15 PVA fibers.

Table 6. Mix proportions by weight of selected ECCs.

Mix	PVA-ECC	LW-ECC	HF-ECC	SHCC/ECC
Reference	(Douglas and Billington 2005)	(Wang and Li 2003)	(Maalej et al. 2005)	(Mechtcherine et al. 2011)
Cement	1.00	1.00	1.00	1.00
Sand (diameter < 0.2 mm)	0.71	0	0	1.06
Glass bubble S60 (3M Co.)	0	0.20	0	0
Silica fume	0	0	0.10	0
Fly ash	0.43	0	0	1.21
Water	0.56	0.45	0.28	0.64
Methylcellulose[1]	0.0027	0.0015	0	0
Superabsorbent polymer[2]	0	0	0	0.0040
Viscosity agent	0	0	0	0.0063
Superplasticizer	0.003	0.03	0.02	0.0328
Fibers [type] (vol %)	2 [PVA]	2 [REC15 PVA]	0.5 [Steel] 1.5 [PE]	2.2 [REC15 PVA]

[1]Methylcellulose is added to reduce fiber settling during mixing and casting (Douglas and Billington 2005).

[2]Superabsorbent polymer is added to reduce autogenous shrinkage, improve freeze-thaw resistance, and introduce microdefects to encourage multiple cracking (Mechtcherine et al. 2011).

3   Material Properties

3.1   Ductal®

Ductal® is perhaps the most well-represented UHPC in the literature and was previously used in multiple projects in North America, including highway bridges in Wapello County (Bierwagen and Abu-Hawash 2005) and Buchanan County (Keierleber et al. 2007), Iowa, as well as a pedestrian bridge in Sherbrooke, Quebec (Blais and Couture 1999). The following section presents data from the literature on dynamic tensile strength, dynamic compressive strength, and preliminary figures on fracture energy. The highest strain rates achieved were 19 s^{-1} in tension and 267 s^{-1} in compression.

3.1.1   Dynamic tensile strength

Published research on Ductal® in dynamic tension (Fujikake et al. 2006; Weckert et al. 2011) deals with relatively low strain rates of 1.0 × 10^{-6} to 19 s^{-1}. Tensile strengths and dynamic increase factors (DIFs) from their work are summarized in Table 7. A DIF of 1.00 corresponds to the static loading rate used as a reference for the other loading rates.

Table 7. Dynamic tensile strength of Ductal®.

No. of tests	Stress Rate (ksi/s)	Strain Rate[1] (s^{-1})	Tensile Strength (ksi)		DIF	Reference
			Average	St. Dev.		
3	——	1.0×10^{-6}	1.64	0.10	1.00	(Fujikake et al. 2006)
3	——	2.0×10^{-3}	1.95	0.22	1.20	
3	——	0.02	2.14	0.18	1.31	
3	——	0.05	2.84	0.25	1.74	
4	0.0145	1.9×10^{-6}	2.2	——	1.00	(Weckert et al. 2011)
3	14.5	1.9×10^{-3}	3.0	——	1.35	
5	1.45×10^{5}	19	3.6	——	1.58	

[1]Only stress rates were given in Weckert et al. (2011). The approximate equivalent strain rate was calculated assuming E = 7650 ksi (Graybeal 2006).

—— indicates no data available

Fujikake et al. (2006) performed uniaxial tension tests using a servo-controlled load frame on square prismatic specimens measuring 2 x 2 x 4 in. Specimens had a notch 0.5 in. deep and 0.12 in. wide cut into either side at the midpoint of the specimen's length. Specimens were cured at 194°F for 2 days after demolding.

Weckert et al. (2011) performed diametric tension tests, also known as split or Brazilian tension tests, using a split Hopkinson pressure bar (SHPB). Specimens were disk-shaped, with a nominal thickness of .25 in. and a nominal diameter of 0.8 in. The curing regime was not specified. As noted above, Weckert et al. reported loading rate in terms of stress rate due to concerns about converting to strain rate, since the elastic modulus is also rate-dependent. For convenience, an approximate equivalent strain rate is also provided.

Relationships between the strain rate and the tensile DIF for Ductal® were given in Fujikake et al. (2006). For strain rates from 1.0×10^{-6} to 5.0×10^{-1} s^{-1}, Fujikake et al. suggests

$$DIF = \frac{f_{td}}{f_{ts}} = \left(\frac{\dot{\varepsilon}}{\dot{\varepsilon}_{st}}\right)^{0.0013\left[\log\left(\frac{\dot{\varepsilon}}{\dot{\varepsilon}_{st}}\right)\right]^{1.95}} \tag{1}$$

where f_{td} is the dynamic tensile strength (MPa); f_{ts} is the static tensile strength, taken as 10.8 MPa; $\dot{\varepsilon}$ is the strain rate (s^{-1}); and $\dot{\varepsilon}_{st}$ is the static strain rate, taken as 1.0×10^{-6} s^{-1}.

Building on the work of Malvar and Ross (1998), Ngo and Mendis (2008) use the relationship

$$DIF = \frac{f_{td}}{f_{ts}} = \left(\frac{\dot{\varepsilon}}{\dot{\varepsilon}_s}\right)^{1.016\delta} \quad \text{for } \dot{\varepsilon} \leq 1 \text{ s}^{-1}$$

$$DIF = \frac{f_{td}}{f_{ts}} = \beta \left(\frac{\dot{\varepsilon}}{\dot{\varepsilon}_s}\right)^{\frac{1}{3}} \quad \text{for } 1 \text{ s}^{-1} < \dot{\varepsilon} \leq 160 \text{ s}^{-1} \tag{2}$$

where f_{td} and f_{ts} are the dynamic and static tensile strengths, respectively (MPa); $\dot{\varepsilon}$ is the strain rate (s^{-1}); $\dot{\varepsilon}_s$ is the quasi-static strain rate, $\dot{\varepsilon}_s = 10^{-6}$ s^{-6}; $\log \beta = 6\delta - 2$; and

$$\delta = \frac{1}{8 + \frac{8f'_{cs}}{10 \text{ MPa}}} \tag{3}$$

where f'_{cs} is the static compressive strength of concrete (MPa).

These two proposed relationships are compared in Figure 1. As both are empirical relationships, they are plotted only for the strain rates for which they were developed. The relationship developed by Fujikake et al. (2006), equation (1), shows dynamic effects becoming noticeable between strain rates of 10^{-3} s and 10^{-2} s, whereas Ngo and Mendis (2008), equation (2), show virtually no increase until 1 s^{-1}. The experimental data for Ductal® (Table 7) are plotted for comparison.

Figure 1. DIF for Ductal® in tension.
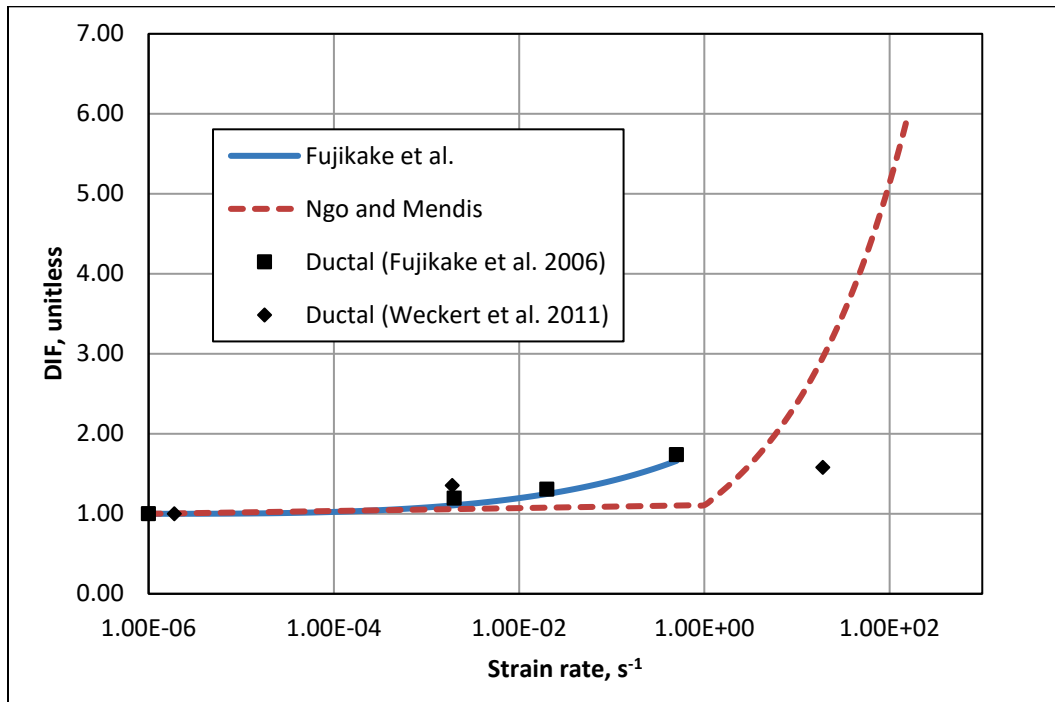
3.1.2 Dynamic compressive strength

SHPB testing performed on Ductal® (Cavill et al. 2006) produced the data for compressive strengths shown in Table 8. The specimens used were cylinders with a diameter of 2 in. After demolding, specimens were steam-cured at 194°F for 48 hr. The static compressive strength of Ductal® was also measured and reported for comparison.

Table 8. Dynamic compressive strength of Ductal® (Cavill et al. 2006).

Test	Average Strain Rate (s^{-1})	Ultimate Compressive Strength (ksi)	DIF
Static	(not given)	23.2	1.00
RPC-1	80.7	27.1	1.17
RPC-2	187.3	32.8	1.41
RPC-3	267.4	34.9	1.51

Based on these data, Ngo and coworkers (Ngo and Mendis 2008; Ngo et al. 2007b) proposed the following equation for the compressive DIF:

$$DIF = \frac{f'_{cd}}{f'_{cs}} = \left(\frac{\dot{\varepsilon}}{\dot{\varepsilon}_s}\right)^{1.026\alpha} \quad \text{for } \dot{\varepsilon} \leq \dot{\varepsilon}_1$$

$$DIF = \frac{f'_{cd}}{f'_{cs}} = A_1 \ln(\dot{\varepsilon}) - A_2 \text{ for } \dot{\varepsilon} > \dot{\varepsilon}_1$$

(4)

where f'_{cd} is the dynamic peak stress (MPa); f'_{cs} is the static compressive strength (MPa); $\dot{\varepsilon}$ is the strain rate (s⁻¹); $\dot{\varepsilon}_s$ is the quasi-static strain rate, $\dot{\varepsilon}_s = 3 \times 10^{-5}$ s⁻¹; $\alpha = 1/(20 + f'_{cs}/2)$; $\dot{\varepsilon}_1$ is the turning-point strain (s⁻¹), $\dot{\varepsilon}_1 = 0.0022(f'_{cs})^2 - 0.1989f'_{cs} + 46.137$; $A_1 = -0.0044f'_{cs} + 0.9866$; and $A_2 = -0.0128f'_{cs} + 2.1396$. Note that, while the calculation of the various parameters is somewhat tedious, they can all be expressed in terms of the static compressive strength.

The proposed relationship for the compressive DIF of Ductal® (equation [4]) is plotted along with experimental data in Figure 2. Although there are only three data points from dynamic testing, the model fits them well.

Figure 2. DIF for Ductal® in compression.
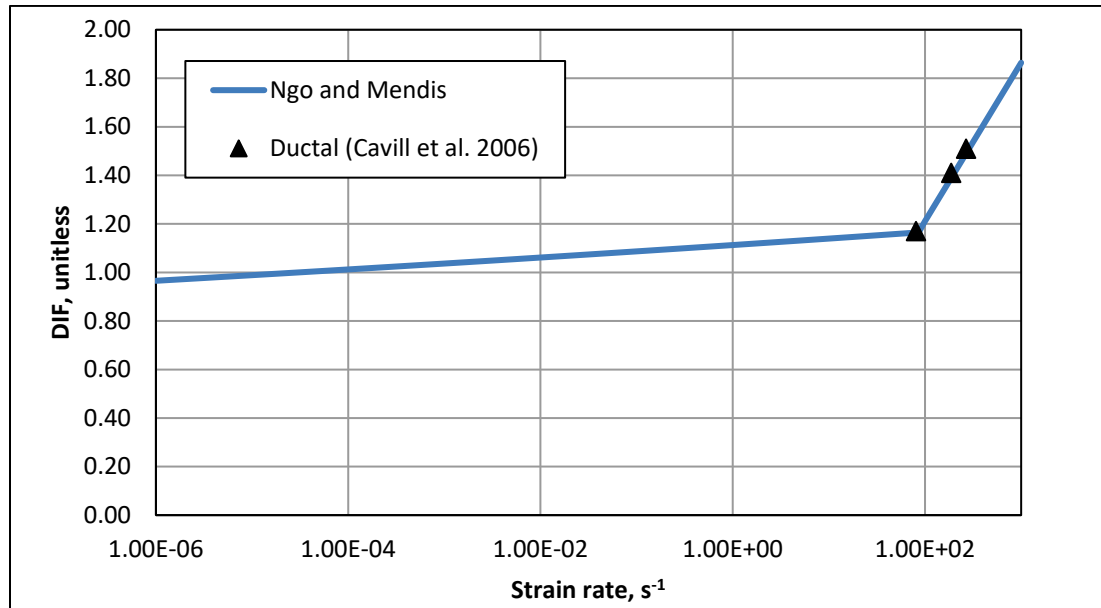
3.1.3 Fracture energy

Studies on the fracture energy of Ductal® under dynamic conditions were difficult to find in the literature. Shaheen and Shrive (2007) did investigate the fracture properties of Ductal® under static conditions. Tests were performed on prismatic specimens measuring 1.6 × 1.6 × 6.3 in. Specimens were made of Ductal® reinforced with ½ in. PVA fibers, rather than the typically used steel fibers. Three notched and three unnotched specimens were tested in four-point bending over a span of 4.3 in. The notch was 0.4 in. deep and 0.04 in. wide and located on the tensile (bottom) face of the specimen. The curing regime was not specified. The reported fracture energy for mode I failure is 1.8 (lbf·in.)/in.² This seems low compared to Densit, for example, which may differ because of the testing methodology (four-point bending vs. SHPB). Note also that this is a static value. The critical J-integral J_{IC} is 74.3 (lbf·in.)/in.² The total energy absorbed by the specimen at fracture was 26.9 lbf·in., or 2663 (lbf·in.)/in.³ on a per-volume basis.

Richard and Cheyrezy (1995), who worked on RPC, the precursor to Ductal®, at Bouygues, gives an approximate static fracture energy of 114.2 lbf·in/in.² for RPCs with compressive strength in the range of 24-33 ksi. Ductal® has an average compressive strength of 28 ksi (Graybeal 2006).

The large difference between the two fracture energies highlights the need for a more thorough investigation of Ductal®'s dynamic fracture properties.

3.1.4 Summary

Ductal® exhibits a tensile strength ranging from 1.64 ksi in static conditions ($\dot{\varepsilon} = 10^{-6}$ s⁻¹) to 3.6 ksi in dynamic conditions ($\dot{\varepsilon} = 19$ s⁻¹). Compressive strength ranges from 23.2 ksi in static conditions to 34.9 ksi in dynamic conditions ($\dot{\varepsilon} = 267.4$ s⁻¹). Relationships for both tensile and compressive DIF as a function of strain rate were presented from the work of Ngo and coworkers (Ngo and Mendis 2008; Ngo et al. 2007b). Insufficient data were available on dynamic fracture energy to make any judgments about fracture behavior.

3.2 Densit

This section presents findings from the literature on the dynamic tensile strength, compressive strength, and fracture energy of Densit. The highest strain rates achieved were around 20 s⁻¹.

3.2.1 Dynamic tensile strength

Ulfkjær et al. (1998) tested three types of UHPC manufactured by Densit ApS (Denmark). Tests were performed using an SHPB setup with a pretensioned bar, causing a tensile pulse to propagate through the incident bar, specimen, and transmission bar. Unfortunately, little is known about the test specimens other than the names of the products used to create the mixes. The specimen geometry and curing regime were not reported. Tests were conducted at strain rates of about 20 s^{-1}. Average tensile strengths from Ulfkjær et al. (1998) are tabulated in Table 9.

Table 9. Dynamic tensile strength of Densit® (Ulfkjær et al. 1998).

Specimen	No. of Tests	Average Tensile Strength (ksi)
Ducorit® D4	2	2.57
Ducorit® S5	2	2.17
Flexbinder	2	2.72

The relationship between strain rate and the tensile DIF for this material does not seem to have been explored in the literature. A relationship similar to one in CEB-FIP 90 (1993) could provide a first approximation. However, this approach is primarily for normal-strength concrete and is not likely to be accurate for UHPC.

3.2.2 Dynamic compressive strength

Solomos and Berra (2004) tested Densit® Ducorit® S5 and Densit® Flexbinder specimens in dynamic compression. At quasi-static strain rates (1×10^{-6} s^{-1}), testing was performed in a load frame; for the other, higher strain rates, the JRC-Ispra modified Hopkinson bar (Cadoni et al. 2006) was used. Specimens were wet-cured for a minimum of 7 days and dried in an outdoor environment for 4-6 weeks. Both 1.57 in. and 2.36 in. cubes were tested. However, results from only the 2.36 in. cubes are presented here; as noted in Graybeal (2006), material heterogeneities have a proportionally larger influence on results from smaller specimens. Average compressive strengths and DIFs at various strain rates from Solomos and Berra (2004) are presented in Table 10.

Table 10. Dynamic compressive strength of Densit® (Solomos and Berra 2004).

Specimen	No. of Tests	Strain Rate (s^{-1})	Average Compressive Strength (ksi)	DIF
Ducorit® S5	3	1×10^{-6}	16.2	1.00
Ducorit® S5	2	1×10^{-3}	27.5	1.69
Ducorit® S5	2	~20	27.8	1.71
Flexbinder	3	1×10^{-6}	27.1	1.00
Flexbinder	2	1×10^{-3}	34.4	1.27
Flexbinder	2	~20	33.9	1.25

It is interesting to note that the lower-strength Ducorit® S5 exhibits greater rate sensitivity than the stronger Flexbinder. The Flexbinder tests at about 20 s^{-1} show a slight decrease in compressive strength, but the sample size is not large enough to determine if this is significant.

3.2.3 Fracture energy

Ulfkjær et al. (1998) also measured the fracture energy of Densit® UHPC specimens under dynamic tension at about 20 s^{-1}. Average values from their data are given in Table 11.

Table 11. Fracture energy of Densit® in dynamic tension (Ulfkjær et al. 1998).

Specimen	No. of Tests	Average Fracture Energy ((lbf·in.)/in.^{2})
Ducorit® D4	2	16.71
Ducorit® S5	2	11.15
Flexbinder	2	33.78

Flexbinder, which was originally designed for protective castings around ATMs, has a fracture energy exceeding those of Ducorit® D4 and S5 by 102% and 203%, respectively.

3.2.4 Summary

Flexbinder had the highest mechanical performance of the three Densit® products researched. Its average dynamic tensile strength was 2.72 ksi. Compressive strength ranged from 27.1 ksi in static conditions ($\dot{\varepsilon} = 10^{-6}$ s^{-1}) to 33.9 ksi in dynamic conditions ($\dot{\varepsilon} \approx 20$ s^{-1}). The average dynamic fracture energy was 33.78 (lbf·in.)/in.^{2}

Ducorit® S5 had the lowest mechanical performance of the three Densit® products researched. Its average dynamic tensile strength was 2.17 ksi. Compressive strength ranged from 16.2 ksi in static conditions

($\dot{\varepsilon} = 10^{-6}$ s^{-1}) to 27.8 ksi in dynamic conditions ($\dot{\varepsilon} \approx 20$ s^{-1}). The average dynamic fracture energy was 11.15 (lbf·in.)/in.^{2}

3.3 B4Q/B5Q

The following section presents data from the literature on the dynamic tensile strength, fracture energy, and elastic modulus of B4Q and B5Q. The highest strain rate achieved was about 160 s^{-1}.

3.3.1 Dynamic tensile strength

Researchers at the University of Kassel (Thoma et al. 2012; Millon et al. 2009; Nöldgen et al. 2013) have performed a large number of SHPB tests on their previously developed UHPCs, B4Q and B5Q (see Section 2.3 for mix design). The curing regime was not specified, although Fehling et al. (2005) describes curing regimes used in previous research at the University of Kassel. SHPB experimentation was conducted according to the methods established by Schuler (Schuler 2004; Schuler and Hansson 2006; Schuler et al. 2006). All specimens were cylinders 3 in. in diameter and 10 in. long. Results are presented in Table 12. Interestingly, the data for all B4Q tests show an initial dip in DIF before the DIF increases again.

As noted by Nöldgen et al. (2013), special care was taken to avoid edge effects on the cylinders. Accordingly, the cylinders were cored from a square panel, 23.6 × 23.6 in. across and 12.6 in. deep, with six cores taken from each panel. The direction of concrete placement was parallel to the cylinders' axes. After drilling, the cylinder ends were shortened by 1.38 in. and ground parallel.

Table 12. Dynamic tensile strength of B4Q and B5Q.

Mix/Fiber Content (vol %)	No. of Tests	Strain Rate (s^{-1})	Tensile Strength (ksi)	DIF	Reference
B4Q/0	2	103	5.92	4.75	(Nöldgen et al. 2013)
B4Q/0	1	111	5.64	4.52	
B4Q/0	2	114	5.63	4.51	
B4Q/0	1	122	6.70	5.37	
B4Q/1.0	1	111	6.06	4.49	(Nöldgen et al. 2013)
B4Q/1.0	1	115	5.67	4.20	
B4Q/1.0	1	129	6.22	4.61	
B4Q/1.0	1	164	6.84	5.08	
B4Q/1.0	1	98.4	7.48	5.52	(Millon et al. 2009)
B4Q/1.0	1	110.7	6.06	4.47	
B4Q/1.0	1	114.5	5.67	4.19	

Mix/Fiber Content (vol %)	No. of Tests	Strain Rate (s⁻¹)	Tensile Strength (ksi)	DIF	Reference
B4Q/1.0	1	129.4	6.22	4.59	
B4Q/1.0	1	131.0	6.74	4.98	
B4Q/1.0	1	135.4	7.34	5.42	
B4Q/1.0	1	137.4	6.65	4.91	
B4Q/1.0	1	163.9	6.85	5.06	
B5Q/2.5	1	132	7.42	4.88	(Nöldgen et al. 2013)
B5Q/2.5	1	148	7.80	5.12	
B5Q/2.5	1	156	8.83	5.80	

For calculating the DIF based on strain rates, Nöldgen et al. (2013) found that the modified CEB-FIP model of Malvar and Ross (1998) fit their data reasonably well. The relationship is

$$DIF = \frac{f_{td}}{f_{ts}} = \left(\frac{\dot{\varepsilon}}{\dot{\varepsilon}_s}\right)^{\delta} \qquad \text{for } 10^{-6}\text{ s}^{-1} \leq \dot{\varepsilon} \leq 1\text{ s}^{-1}$$

$$DIF = \frac{f_{td}}{f_{ts}} = \beta \left(\frac{\dot{\varepsilon}}{\dot{\varepsilon}_s}\right)^{\frac{1}{3}} \qquad \text{for } 1\text{ s}^{-1} < \dot{\varepsilon} \leq 160\text{ s}^{-1}$$

(5)

where f_{td} and f_{ts} are the dynamic and static tensile strengths, respectively (MPa); $\dot{\varepsilon}$ is the strain rate (s⁻¹); $\dot{\varepsilon}_s$ is the quasi-static strain rate, $\dot{\varepsilon}_s = 10^{-6}\text{s}^{-6}$; $\log \beta = 6\delta - 2$; and

$$\delta = \frac{1}{1 + \frac{8f'_{cs}}{10\text{ MPa}}}$$

(6)

where f'_{cs} is the static compressive strength of concrete (MPa).

The DIF relationship for B5Q with 2.5 vol % steel fibers (equation [5]) is shown in Figure 3. For comparison, the experimental data are also plotted.

Figure 3. DIF for B5Q (2.5 vol % fibers) in tension.
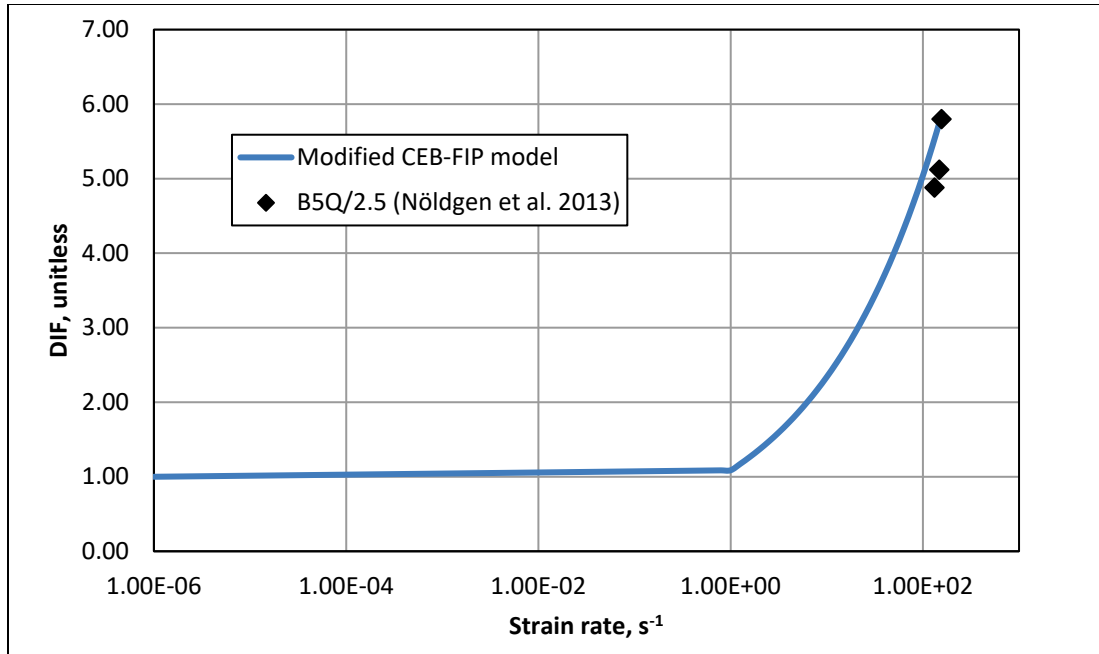
3.3.2 Fracture energy

Millon et al. (2009) measured the dynamic fracture energy of B4Q with 1.0-vol % steel fibers at multiple strain rates. Their experimental values and calculated DIFs are reported in Table 13. As noted above, tests were performed using an SHPB, with methods previously described by Schuler (Schuler 2004; Schuler and Hansson 2006; Schuler et al. 2006).

Table 13. Fracture energy of B4Q in dynamic tensile testing (Millon et al. 2009).

Strain Rate (s^{-1})	Fracture Energy (($lbf \cdot in.$)/$in.^2$)	DIF
129.2	85.14	1.49
129.3	42.97	0.75
144.3	73.72	1.29
144.5	51.49	0.90
164.0	65.15	1.14

There is significant scatter in the data above, with wide variance even at similar strain rates.

Additionally, researchers at the University of Kassel (Thoma et al. 2012; Millon et al. 2009; Nöldgen et al. 2013) have averaged the fracture energy values obtained for each UHPC mix under high strain-rate tensile testing. These data are summarized in Table 14.

Table 14. Average fracture energy of B4Q and B5Q in dynamic tensile testing.

Mix/Fiber Content (vol %)	Average Fracture Energy ([lbf·in.]/in.^{2})	Reference
B4Q/1.0	63.67	(Millon et al. 2009)
B4Q/1.0	57.50	(Nöldgen et al. 2013)
B5Q/2.5	64.47	
B4Q/0	2.06	(Thoma et al. 2012)
B4Q/1.0	64.01	
B5Q/2.5	80.97	

Although values varied between the tests performed by different authors, the fracture energy increased significantly with the addition of 1.0 vol % fibers. Increasing to 2.5 vol % fibers further increased fracture energy.

3.3.3 Elastic modulus

Millon et al. (2009) measured the dynamic elastic modulus of B4Q with 1.0-vol % steel fibers at multiple strain rates. Their experimental values and calculated DIFs are reported in Table 15. For comparison, the static elastic modulus is given as 7736 ksi (Millon et al. 2009). Over the range of strain rates tested, elastic modulus seems to show very little rate-dependence, with the DIF fluctuating between 0.96 and 1.09.

Table 15. Elastic modulus of B4Q in dynamic tensile testing (Millon et al. 2009).

Strain Rate (s^{-1})	Elastic Modulus (ksi)	DIF
98.4	8327	1.08
110.7	7441	0.96
114.5	8398	1.09
129.4	7536	0.97
131.0	8339	1.08
135.4	8368	1.08
137.4	8413	1.09
163.9	7427	0.96

The relative performance of the different UHPC mixes can be assessed by the average dynamic elastic moduli given by Thoma et al. (2012), Millon et al. (2009), and Nöldgen et al. (2013) and is summarized in Table 16.

Table 16. Average elastic moduli of B4Q and B5Q in dynamic tensile testing.

Mix/Fiber Content (Vol %)	Average Elastic Modulus (ksi)	Reference
B4Q/1.0	8031	(Millon et al. 2009)
B4Q/0	7337	(Nöldgen et al. 2013)
B4Q/1.0	7700	
B5Q/2.5	8207	
B4Q/0	7091	(Thoma et al. 2012)
B4Q/1.0	7830	
B5Q/2.5	8019	

3.3.4 Summary

The greatest amount of data was available for B4Q with 1.0 vol % steel fibers. Its tensile strength ranged from 1.35 ksi in static conditions to 6.84 ksi in dynamic conditions ($\dot{\varepsilon}$ = 156 s^{-1}). Dynamic fracture energy showed a large amount of scatter over the strain rates tested (129-164 s^{-1}), with fracture energy ranging from 42.97 to 85.14 (lbf·in.)/in.^{2} Dynamic elastic modulus also fluctuated over the range tested (98-164 s^{-1}), with the lowest and highest values, 7427 and 8413 ksi, occurring at 163.9 and 137.4 s^{-1}, respectively.

The best mechanical performance came from B5Q with 2.5 vol % steel fibers. Its tensile strength ranged from 1.52 ksi in static conditions to 8.83 ksi in dynamic conditions ($\dot{\varepsilon}$ = 156 s^{-1}). Its average dynamic fracture energy was between 64.47 and 80.97 (lbf·in.)/in.^{2}, and its average dynamic elastic modulus was between 8019 and 8207 ksi.

3.4 UHPCC

The following section presents dynamic compressive strength, energy absorption, strain at peak stress, and elastic modulus data from the literature on UHPCC. The highest strain rate achieved was roughly 96 s^{-1}.

3.4.1 Compressive strength

Rong et al. (2010) and Lai and Sun (2009) investigated the dynamic behavior of UHPCC with varying amounts of steel fiber. Tests were performed with an SHPB and cylindrical specimens. Specimens had a diameter of 2.76 in. and were 1.38 in. long. Specimens were demolded after 24 hr and cured at 68°F and RH > 90% for 60 days before testing. Results are summarized in Table 17. DIFs were calculated using static compressive strengths at 60 days given in both works (Rong et al. 2010; Lai and Sun 2009).

Table 17. Dynamic compressive strength of UHPCC.

Fiber Content (vol %)	Strain Rate (s⁻¹)	Compressive Strength (ksi)	DIF	Reference
0	25.9	19	0.90	(Rong et al. 2010)
0	36.2	19	0.94	
0	55.1	24	1.16	
0	82.5	29	1.39	
3	32.1	20	0.75	
3	41.9	24	0.88	
3	69.2	26	0.95	
3	93.4	28	1.02	
4	32.1	25	0.84	
4	50.8	27	0.91	
4	86.1	28	0.96	
4	92.9	29	0.99	
0	24.9	20.0	0.97	(Lai and Sun 2009)
0	30.8	20.6	0.99	
0	38.3	25.8	1.24	
0	87.2	29.0	1.40	
3	31.6	21.3	0.79	
3	38.8	22.5	0.83	
3	66.8	25.8	0.96	
3	99.2	27.8	1.03	
4	23.7	21.8	0.74	
4	44.0	25.4	0.86	
4	67.1	28.9	0.98	
4	95.8	29.4	1.00	

Peculiarly, all UHPCC mix types show a DIF < 1.00 at lower strain rates. While the compressive strength does increase, the DIF appreciably exceeds 1.0 only in the specimens without fiber reinforcement. This is seen in the plot of the compression test data in Figure 4. This behavior warrants further research if UHPCC is to be considered for use in blast protection.

Lai and Sun (2008; 2010) also investigated the dynamic properties of UHPCC under repeated compressive impact loads with SHPB. Specimens

had a diameter of 2.76 in. and were 1.38 in. long. Specimens were demolded after 24 hr and cured at 68°F and RH > 90% for 60 days before testing.

Figure 4. Comparison of DIFs for UHPCC in compression.
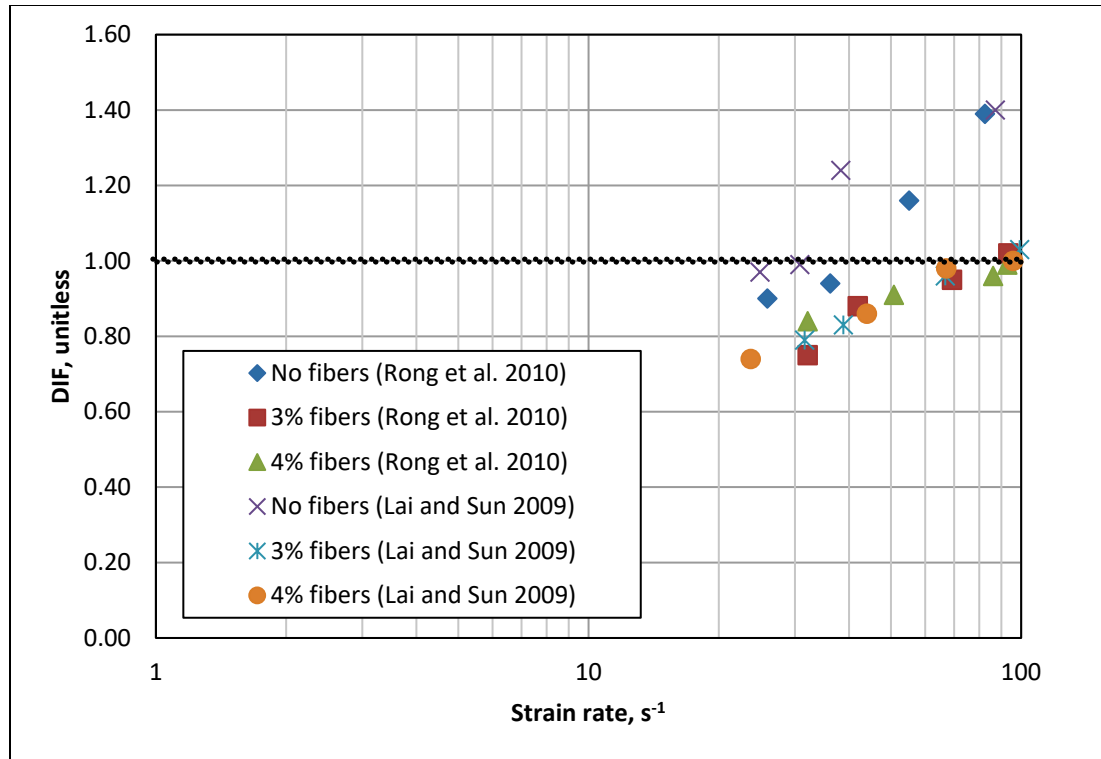
A stress-strain relationship that accounts for the strain rate was proposed by Lai and Sun (2009) based on the visco-elastic ZWT model (Wang et al. 1996; Wang 2007) and incorporating a material damage parameter based on elastic modulus degradation (Lemaitre and Chaboche 1990; Mehta and Monteiro 2006). The resulting visco-elastic damage model describes material response under the impact testing performed:

$$\sigma = (1 - D)\left[E\varepsilon + E_2\theta_2\dot{\varepsilon}\left(1 - \exp\left(-\frac{\varepsilon}{\dot{\varepsilon}^{\theta_2}}\right)\right)\right] \tag{7}$$

and

$$D = 1 - \frac{E_1}{E_0} = 1 - \frac{V_1^2}{V_0^2} \tag{8}$$

where D is the unitless material damage parameter; E and E_2 are fitting parameters describing the elastic properties of the material at low and high strain rates, respectively (ksi or MPa); θ_2 is a fitting parameter

representing the material's relaxation time (μs); $\dot{\varepsilon}$ is the strain rate (s⁻¹); E_0 and E_1 are the elastic moduli of the material before and after the impact, respectively (ksi or MPa); and V_0 and V_1 are the ultrasonic wave velocities of the material before and after the impact, respectively (ft/s or m/s).

Rong et al. (2010) noted that the Johnson_Holmquist_Concrete model in LS-DYNA corresponded well with their experimental data and could be used for future simulation of UHPCC in dynamic compression.

3.4.2 Energy absorption

Lai and Sun (2009) did not report fracture energies for the UHPCC specimens, although they did give the energy absorbed by the specimens on a per-volume basis. Their data are presented in Table 18. In some cases, this energy absorption corresponds to the modulus of toughness; however, the fiber-reinforced specimens did not fracture even at the highest strain rate.

Table 18. Energy absorption of UHPCC under dynamic compressive testing (Lai and Sun 2009).

Fiber Content (vol %)	Strain Rate (s⁻¹)	Energy Absorbed (lbf·in./in.³)
0	24.9	74
0	30.8	195
0	38.3	203
0	87.2	304
3	31.6	48
3	38.8	146
3	66.8	206
3	99.2	456
4	23.7	50
4	44.0	90
4	67.1	217
4	95.8	440

3.4.3 Strain at peak stress

Data are also available on the strain at peak stress for the UHPCC specimens tested by Lai and Sun (2008; 2009). In Lai and Sun (2008), specimens were subjected to repeated impact at progressively higher strain rates. Because the specimen incurred significant damage during this process, only data for undamaged specimens under the first impact are reported from that study. Batches with coarse aggregate are noted as such in the table below. Peak strain values are given in Table 19.

Table 19. Strain at peak stress for UHPCC under dynamic compressive testing.

Fiber Content (vol %)	Strain Rate (s⁻¹)	Strain at Peak Stress ($\times 10^{-6}$)	Reference
0	24.9	3588	(Lai and Sun 2009)
0	30.8	3340	
0	38.3	3923	
0	87.2	4883	
3	31.6	4290	
3	38.8	4421	
3	66.8	5575	
3	99.2	6308	
4	23.7	3281	
4	44.0	4619	
4	67.1	5570	
4	95.8	5808	
0	24.9	3588	(Lai and Sun 2008)
3	35.4	4518	
4	23.7	3270	
0 [1]	19.4	2768	
2 [1]	25.2	3427	
3 [1]	33.8	4070	

[1]Mix includes coarse aggregates (see Section 2.4).

3.4.4 Elastic modulus

Lai and Sun (2008; 2009) also reported on elastic moduli of UHPCC under dynamic compressive loading. Their data are presented in Table 20. Specimens were prepared for testing as described in Section 3.4.1. As before, the results reported from Lai and Sun (2008) are for undamaged specimens. Also, some of the mixes in that study incorporated coarse aggregates; these are noted as such in the table below.

No DIFs could be calculated for the first set of data (Lai and Sun 2009), though the DIFs for Lai and Sun (2008) show a similar trend, as noted earlier in Section 3.4.1, where the dynamic performance is actually inferior to that in static situations. Only for the case of UHPCC with coarse aggregate and no fiber reinforcement is the performance the same.

Table 20. Elastic modulus of UHPCC in dynamic compressive testing.

Fiber Content (Vol %)	Strain Rate (s^{-1})	Elastic Modulus (ksi)	DIF	Reference
0	24.9	7265	(No data for static elastic modulus from this source.)	(Lai and Sun 2009)
0	30.8	7816		
0	38.3	7656		
0	87.2	8410		
3	31.6	6859		
3	38.8	7192		
3	66.8	7787		
3	99.2	8323		
4	23.7	7511		
4	44.0	8077		
4	67.1	8294		
4	95.8	8729		
0	24.9	7265	0.92	(Lai and Sun 2008)
3	35.4	7062	0.85	
4	23.7	8019	0.96	
0 [1]	19.4	8193	1.00	
2 [1]	25.2	7526	0.91	
3 [1]	33.8	7468	0.88	

[1]Mix includes coarse aggregates (see Section 2.4).

3.4.5 Summary

UHPCC with 3 vol % steel fibers had a dynamic compressive strength that ranged from 20–28 ksi at strain rates of 32-94 s^{-1}. Energy absorption during impact tests ranged from 48-456 (lbf·in.)/in.^{2} at strain rates of 32-99 s^{-1}. The strain at peak stress ranged from 4290-6308 ($\times$ 10^{-6}) at strain rates of 32–99 s^{-1}. Finally, the dynamic elastic modulus ranged from 6859-8323 ksi at strain rates of 32-99 s^{-1}.

UHPCC with 4 vol % steel fibers had a dynamic compressive strength that ranged from 25-29 ksi at strain rates of 32-93 s^{-1}. Energy absorption during impact tests ranged from 50-440 (lbf·in.)/in.^{2} at strain rates of 23-96 s^{-1}. The strain at peak stress ranged from 3281-5808 ($\times$ 10^{-6}) at strain rates of 24-96 s^{-1}. Finally, the dynamic elastic modulus ranged from 7511-8729 ksi at strain rates of 24-96 s^{-1}.

3.5 CEMTEC_{multiscale}®

While less information is available about the dynamic properties of CEMTEC_{multiscale}®, it is perhaps the most well-established in the category of multiscale fiber-reinforced concrete (MSFRC). For the data in this section, the maximum strain rate achieved was about 12 s^{-1}.

3.5.1 Dynamic tensile strength and modulus of rupture

Rossi, Parant, and others have investigated the dynamic properties of CEMTEC_{multiscale}® in impact loading (Parant et al. 2007; Rossi and Parant 2008). Modulus of rupture testing was performed in four-point bending using the block-bar device developed in the Laboratoire de Mécanique des Matériaux et des Structures at the University of Lyon and described in detail elsewhere (Jacquelin and Hamelin 2001). The device uses a compressed-air gun to launch a mass into a specimen, or a load applicator placed on the specimen. In this case, a 110 lb mass was launched at about 12.5 mph onto a fixture that applied loads at third-points on the specimen (Parant et al. 2007). Specimens were 23.6 in. long, 7.9 in. wide, and 1.6 in. high. After demolding, specimens were left in laboratory conditions for 48 hr before heat treatment in a drying oven at 194°F for 4 days. Results from both papers are summarized in Table 21.

Table 21. Dynamic tensile strength and modulus of rupture of CEMTEC$_{multiscale}$®.

Stress Rate (ksi/s)	Elastic Modulus[1] (ksi)	Strain Rate[1] (s^{-1})	Modulus of Rupture (ksi)	DIF	Tensile Strength (ksi)	Reference
1.81×10^{-2}	7323	2.48×10^{-6}	8.7	1.00	2.9	(Rossi and Parant 2008)
1.81	7511	2.41×10^{-4}	9.7	1.12	3.2	
181	8251	2.20×10^{-2}	10.9	1.25	4.2	
7.25×10^3	8251	0.88	17.7	2.03	(No data)	(Parant et al. 2007)
8.70×10^3	8251	1.05	18.6	2.13		
9.14×10^3	8251	1.11	18.3	2.10		
2.52×10^4	8251	3.06	22.2	2.55		
2.73×10^4	8251	3.30	23.6	2.72		
3.57×10^4	8251	4.32	23.8	2.73		
4.21×10^4	8251	5.10	23.9	2.75		
4.38×10^4	8251	5.31	21.6	2.48		
4.89×10^4	8251	5.92	32.3	3.72		
5.12×10^4	8251	6.20	29.4	3.38		
6.09×10^4	8251	7.38	27.7	3.18		
7.11×10^4	8251	8.61	32.5	3.73		
7.16×10^4	8251	8.68	33.8	3.88		
7.19×10^4	8251	8.72	29.9	3.43		
8.80×10^4	8251	10.7	32.6	3.75		
1.02×10^5	8251	12.3	35.4	4.07		

[1]Only stress rates were reported for the tests. Values for the elastic moduli are taken from Parant et al. (2007) for stress rates ranging from 1.81×10^{-2} to 181 ksi/s. Above these stress rates, the elastic modulus is taken as the elastic modulus at 181 ksi/s. While this likely underestimates the elastic modulus, and therefore overestimates the strain rate, there were insufficient data to make a reasonable determination of the elastic modulus at these higher rates.

3.5.2 Summary

Tensile strength increased from 2.9 ksi at a strain rate of 2.5×10^{-6} s^{-1} to 4.2 ksi at 0.022 s^{-1}. The modulus of rupture increased from 8.7 ksi at a strain rate of 2.5×10^{-6} s^{-1} to 35.4 ksi at 12.3 s^{-1}.

3.6 Engineered cementitious composite

This section presents data on the dynamic tensile and compressive strength of several ECCs, as well as work of fracture and elastic modulus for SHCC/ECC. The highest strain rate achieved was 50 s^{-1}.

3.6.1 Dynamic tensile strength

Various researchers (Douglas and Billington 2005; Maalej et al. 2005; Yang and Li 2005; Mechtcherine et al. 2011) have investigated concretes classified

as ECCs. Their results are summarized in Table 22. Standard deviations are reported when given or when able to be calculated from raw data.

Table 22. Dynamic tensile strength of ECC.

Material	Strain Rate (s^{-1})	Tensile Strength (ksi)		DIF	Reference
		Average	St. Dev.		
PVA-ECC	Quasi-static	0.39	——	1.00	(Douglas and Billington 2005)
	2×10^{-4}	0.44	——	1.11	
	0.02	0.58	——	1.48	
	0.2	0.70	——	1.78	
LW-ECC	2×10^{-5}	0.62	——	1.00	(Yang and Li 2005)
	0.002	0.71	——	1.14	
	0.1	0.81	——	1.30	
HF-ECC	2×10^{-6}	0.45	0.05	1.0	(Maalej et al. 2005)
	2×10^{-5}	0.48	0.04	1.1	
	2×10^{-4}	0.53	0.08	1.2	
	0.002	0.67	0.06	1.5	
	0.02	0.68	0.06	1.5	
	0.2	0.87	0.05	1.9	
SHCC/ECC	10^{-5}	0.66	0.07	1.00	(Mechtcherine et al. 2011)
	10^{-4}	0.77	0.09	1.16	
	10^{-3}	0.78	0.06	1.18	
	10^{-2}	0.80	0.08	1.21	
	10	1.13	0.20	1.72	
	25	1.75	0.30	2.66	
	50	1.73	0.12	2.63	

—— indicates no data available.

Douglas and Billington (2005) tested cylinders 2 in. in diameter and 4 in. high. Specimens were demolded at 24 hr, wet cured for 15 days, and allowed to dry for 12 days before testing. The cylinder ends were attached to aluminum end caps using a high-strength epoxy. Uniaxial tensile testing was performed using a 56-kip closed-loop servo-controlled MTS frame under displacement control. Three LVDTs were used to measure displacement.

Yang and Li (2005) tested coupon specimens measuring 8.7 × 3 × 0.5 in. with a gauge length of 4 in. Specimens were tested at 28 days (curing regime not specified). Uniaxial tensile testing was performed using a servohydraulic test frame under displacement control.

Maalej et al. (2005) tested coupon specimens measuring 11.8 × 3 × 0.6 in. with a gauge length of 5.5 in. at approximately 28 days. The curing regime was not specified. Uniaxial tensile testing was performed using an Instron servo-hydraulic test frame under displacement control. Displacement was measured using two LVDTs mounted on a supporting frame.

Mechtcherine et al. (2011) tested dog-bone-shaped specimens. The gauge length was 4 in., with a cross section of 0.94 × 1.57 in. for the gauge length and a cross section of 1.57 x 1.57 in. at the ends. The total length was 10 in. Specimens were left in molds for 2 days and stored in a room kept at 77°F and RH = 65%. After demolding, specimens were sealed in plastic film and stored at room temperature. Low-speed tensile testing (10^{-5} to 10^{-2} s^{-1}) was performed on an Instron servo-hydraulic test frame under displacement control. The specimen ends were attached to steel rings on the grips using a fast-setting HBM glue. Displacements were measured using two LVDTs. High-speed tensile testing (10 to 50 s^{-1}) was performed using a high-rate MTS test frame. Refer to Mechtcherine et al. (2011) or Silva et al. (2010) for more details on the high-speed tensile testing procedure. Six specimens were tested at each strain rate.

3.6.2 Dynamic compressive strength

Douglas and Billington (2005) performed dynamic compressive testing on PVA-ECC (see Section 2.6 for mix information). Average values and DIFs are reported in Table 23. The same specimen types and equipment were used for the tensile testing by the same authors (see Section 3.6.1).

Table 23. Dynamic compressive strength of PVA-ECC (Douglas and Billington 2005).

Strain Rate (s^{-1})	Compressive Strength (ksi)	DIF
Quasi-static	6.6	1.00
2×10^{-4}	6.7	1.02
0.02	7.9	1.20
0.2	8.8	1.34

3.6.3 Work to fracture

Mechtcherine et al. (2011) determined the work to fracture (modulus of toughness) of SHCC/ECC specimens tested at low and high speeds. The specimens and equipment used are the same as in Section 3.6.1. Results are shown in Table 24.

Table 24. Work to fracture of SHCC/ECC under dynamic tensile testing
(Mechtcherine et al. 2011).

Strain Rate (s^{-1})	Work to Fracture (lbf·in.)		DIF
	Average	St. Dev.	
10^{-5}	71.2	22.7	1.00
10^{-4}	68.1	15.0	0.96
10^{-3}	59.4	24.7	0.83
10^{-2}	46.5	23.2	0.65
10	87.3	20.8	1.23
25	93.0	18.3	1.31
50	177.3	20.3	2.49

3.6.4 Elastic modulus

Mechtcherine et al. (2011) also reported dynamic values of the elastic modulus for the dogbone specimens tested at low strain rates (10^{-5} to 10^{-2} s^{-1}). Results are summarized, with DIFs calculated, in Table 25. The elastic modulus dropped slightly from 0.001 to 0.01 s^{-1}. However, the decrease was not statistically significant: two-sample $t(8) = 0.047, p = 0.48$.

Table 25. Elastic modulus of SHCC/ECC in dynamic tensile testing (Mechtcherine et al. 2011).

Strain Rate (s^{-1})	Elastic Modulus (ksi)		DIF
	Average	St. Dev.	
10^{-5}	2851	326	1.00
10^{-4}	3036	502	1.07
10^{-3}	3471	381	1.22
10^{-2}	3463	239	1.21

3.6.5 Summary

PVA-ECC had a tensile strength that ranged from 0.39 ksi in quasi-static conditions to 0.70 ksi at 0.2 s^{-1}, for a DIF of 1.78. Compressive strength showed less rate sensitivity, ranging from 6.6 ksi in quasi-static conditions to 8.8 ksi at 0.2 s^{-1}, for a DIF of 1.34.

SHCC/ECC had the highest tensile strength, ranging from 0.66 ksi at 10^{-5} s^{-1} to 1.73 ksi at 50 s^{-1}, for a DIF of 2.62. No dynamic compression data were available. Work to fracture ranged from 71.2 lbf·in. at 10^{-5} s^{-1} to 177.3 lbf·in. at 50 s^{-1}, for a DIF of 2.49. The elastic modulus ranged from 2851 ksi at 10^{-5} s^{-1} to 3463 ksi at 0.01 s^{-1}, for a DIF of 1.21.

4   Material Comparison

The average tensile strengths, compressive strengths, fracture energies, and elastic moduli of the examined UHPCs are compared in Tables 26 through 29. For each UHPC material, averages are given for each range of strain rates where data were available. The chosen strain rate ranges are 10^{-6} to 10^{-4} s^{-1}, corresponding to quasi-static loading; 10^{-4} to 1 s^{-1}, corresponding to slow and moderate dynamic loading; 1 to 100 s^{-1}, corresponding to impact loading; and 100 s^{-1} and above, corresponding to blast loading (Ngo et al. 2007a). Static values not previously introduced in the material property sections are taken from Thoma et al. (2012) for B5Q and Rossi et al. (2005) for CEMTEC$_{multiscale}$®.

For more accurate comparison, the use of conversion factors to normalize results from different specimen sizes and shapes was attempted. However, these factors depend on many variables, including the strength of concrete used and the type of test. Neville (1966) performed a comprehensive study on conversion factors for NSC in compression. Several studies have addressed conversion between cubes and cylinders (with L/D = 2) for high-strength concrete (HSC) up to UHPC (Mansur and Islam 2002; Yi et al. 2006; Del Viso et al. 2008; Graybeal and Davis 2008), with prisms (L/D = 2) also included in one work (Yi et al. 2006). As can be seen in the results in previous sections, many investigations used unorthodox shapes, including notched prisms and cylinders with aspect ratios (L/D) of 0.31, 0.5, and 3.33. Tests included split-tension, direct tension, three-point bending, four-point bending, and compressive and tensile testing with SHPB. As a result, it was very difficult to find conversion factors for all data. It was decided not to attempt to normalize any properties in this way, since only a portion of all results could be normalized, and partial conversion would render normalization pointless.

4.1   Tensile strength

In terms of tensile strength (Table 26), CEMTEC$_{multiscale}$® had the best performance at strain rates below 100 s^{-1}. Note that the tensile strength for all ranges except the quasi-static were converted from modulus of rupture data using a linear correlation (see note after table). Although a theoretical correlation between tensile strength and modulus of rupture based on beam theory ($\sigma = My/I$) was developed (Raphael 1984), the assumptions break down for UHPC, and the relationship did not describe the data for CEMTEC$_{multiscale}$® well. The values seen are

impressive, but not unheard of, although the inherent inaccuracy of the conversion should be kept in mind. Above 100 s^{-1}, B5Q was the only UHPC with data, so it cannot be compared to the others. Its tensile strength of 24 ksi corresponds to a DIF of about 15.8. ECCs are known for strain-hardening properties and high tensile strain capacity, but the tensile strength of SHCC/ECC was relatively low.

4.2 Compressive strength

In terms of compressive strength (Table 27), B5Q provided the best quasi-static performance. At higher strain rates, Densit® Flexbinder performed best of all the UHPCs with data. It exhibited a slight decrease in strength with strain rate increasing from 10^{-3} to 20 s^{-1}, but the study (Solomos and Berra 2004) did not have enough data points to determine whether this is significant. Unfortunately, B5Q, CEMTEC$_{multiscale}$®, and SHCC do not have data for dynamic compressive strengths. The static compressive strength for SHCC/ECC is taken from Mechtcherine et al. (2012).

4.3 Fracture energy

The available data on fracture energy are quite scarce, as shown in Table 28. UHPCC and SHCC/ECC both have data on work to failure or fracture. However, converting this data to fracture energy requires information on the crack area. Based on the data found to date, no meaningful comparison was possible between the UHPCs.

4.4 Elastic modulus

In terms of elastic modulus (Table 29), Densit® Flexbinder is the stiffest, followed by B5Q. CEMTEC$_{multiscale}$® has the second lowest stiffness, although it is the only UHPC of the three with data at multiple strain rates that do not show decreasing stiffness with increasing strain rate. Unusually, B5Q and UHPCC both decrease in stiffness at higher strain rates. However, the range of strain rates at which the elastic modulus was measured is different for each of the three UHPCs. SHCC/ECC had the lowest elastic modulus by far.

4.5 Remarks

Although no dynamic test data were available for Densit® Inducast TT5, it may still warrant attention for blast protection. It has a nominal static compressive strength of 43 ksi. As an approximate estimate, assuming that other mechanical properties are proportional to $\sqrt{f'_{cs}}$,

as in simplified methods in the ACI 318-11 code (2011), the tensile strength and elastic modulus of Inducast TT5 could be about 10% greater than those of Flexbinder.

As seen in Sections 3.4.1 and 3.4.4, the compressive strength and modulus of elasticity of UHPCC tend to decrease under dynamic conditions. For fiber-reinforced UHPCC, the dynamic compressive strength was 74–103% of the static value; for nonfiber-reinforced UHPCC, the dynamic compressive strength was 90–140% of the static value. Relative to static values, the elastic modulus was between 85–96% for fiber-reinforced UHPCC and 92-100% for nonfiber-reinforced UHPCC.

Table 26. Comparison of average tensile strengths (ksi) of selected UHPCs.

Strain Rate Range (s⁻¹)	Ductal®	Densit® Flexbinder	B5Q, 2.5 Vol % Fibers	UHPCC, 4 Vol % Fibers	CEMTEC$_{multiscale}$®[1]	SHCC/ECC
10^{-6} to 10^{-4}	1.96	—— ——	1.52	——	2.9	0.71
10^{-4} to 1	2.48	——	——	——	5.2 [1]	0.79
1 to 100	3.6	2.72	——	——	13.9 [1]	1.54
Above 100	——	——	24.06	——	——	——

[1]No tensile strength data were available at higher strain rates, so for comparison, tensile strengths (f_t) were extrapolated from the modulus of rupture (f_r) using the least-squares equation for the lower strain rate range, $f_t = 0.60651 f_r - 2.4899$, $r^2 = 0.9279$, with all values in ksi.

—— indicates no data available.

Table 27. Comparison of average compressive strengths (ksi) of selected UHPCs.

Strain Rate Range (s⁻¹)	Ductal®	Densit® Flexbinder	B5Q, 2.5 Vol % Fibers	UHPCC, 4 Vol % Fibers	CEMTEC$_{multiscale}$®	SHCC/ECC
10^{-6} to 10^{-4}	23.2	27.1	30.2	29.6	29.7	8.8
10^{-4} to 1	——	34.4	——	——	——	——
1 to 100	27.1	33.9	——	26.8	——	——
Above 100	33.9	——	——	——	——	——

—— indicates no data available.

Table 28. Comparison of average fracture energies ((lbf·in.)/in.²) of selected UHPCs.

Strain Rate Range (s^{-1})	Ductal®	Densit® Flexbinder	B5Q, 2.5 Vol % Fibers	UHPCC, 4 Vol % Fibers	CEMTEC$_{multiscale}$®	SHCC/ECC
10^{-6} to 10^{-4}	1.8	——	——	——	——	——
10^{-4} to 1	——	——	——	——	——	——
1 to 100	——	33.8	——	——	——	——
Above 100	——	——	90.0	——	——	——

—— indicates no data available.

Table 29. Comparison of average elastic moduli (ksi) of selected UHPCs.

Strain Rate Range (s^{-1})	Ductal®	Densit® Flexbinder	B5Q, 2.5 Vol % Fibers	UHPCC, 4 Vol % Fibers	CEMTEC$_{multiscale}$®	SHCC/ECC
10^{-6} to 10^{-4}	7650	9425	8642	8396	7323	2944
10^{-4} to 1	——	——	——	——	7881	3467
1 to 100	——	——	——	8126	——	——
Above 100	——	——	8113	——	——	——

—— indicates no data available.

5   Applications

5.1   Existing applications

Ductal® was used to fabricate blast-resistant panels for an Australian government facility in a high-risk international location (Rebentrost and Wight 2011). The client was the Department of Foreign Affairs and Trade; the panels were designed and manufactured in a cooperative project between VSL Australia Pty Ltd and the Advanced Protective Technologies for Engineering Structures group at the University of Melbourne (Cavill et al. 2006). The panels were installed on the roof of the building in July 2005 and measured up to 14.8 ft long, 6.6 ft wide, and 4 in. thick. Further details are classified by the Australian government.

ECC panels were tested as blast mitigations by Foust and Oesch (2012); details are not available in the open literature but the report may be obtained by US government agencies and their contractors.

5.2   Structural and sacrificial shielding

Research at ERDC on blast mitigation for steel bridge towers explored the concepts of structural and sacrificial shielding (Walker et al. 2011). A structural shield has sufficient strength, strain energy capacity, and inertial resistance to withstand and reflect the shock wave from a blast. The shield would be integral with the structure that it is designed to protect. However, the amount of energy absorbed by a structural shield would be immense and would require adequate support to prevent the shield from impacting the structure behind it. A sacrificial shield, on the other hand, is designed not to withstand the blast, but to reflect the shock wave, provide inertial resistance, and dissipate energy by breaking up. The shield should be designed so that the kinetic energy transferred to the structure is minimized. Thus, a material with high energy absorption capacity and little to no fragmentation would be ideal. The kinetic energy, KE, imparted to the structure is proportional to

$$KE \propto \frac{i^2}{M} \tag{9}$$

where i is the impulse per unit area (pressure·time) and M is the mass per unit area of both the shield and the target behind it (Walker et al. 2011).

Walker et al. (2011) tested multiple sacrificial shield configurations made of NSC with compressive strengths up to 5.6 ksi and steel rebar and/or fiber reinforcement. In near-contact blasts, it was found that the concrete crushed under the shock wave and flowed hydrodynamically. This resulted in a high-mass, high-velocity flow field impacting the structure. For NSC, results indicated that the crushing and subsequent hydrodynamic flowing were not significantly affected by the flexural strength of the concrete. It is not known whether the same damage mechanism would occur in UHPC under the same conditions. UHPC does have a much higher compressive strength, which may better resist crushing and prevent hydrodynamic flow to the extent seen in NSC.

UHPC has a much greater flexural capacity than NSC, resulting in significantly improved energy absorption and reduced fragmentation. The open literature contains limited data from blast testing of Ductal®. One study that was available, Rebentrost and Wight (2011), reported on blast testing of Ductal® panels with scaled distances of 1.01 to 7.56 ft/lb$^{1/3}$. RC panels were also tested for comparison. Results showed that the Ductal® panels developed a hinge, allowing much greater deformation with little or no fragmentation.

UHPC is also slightly denser than NSC. These factors suggest that UHPC could perform successfully in a sacrificial shield for moderate standoffs or near-contact blasts with smaller charges. It is recommended that tests be conducted to determine under what blast conditions UHPC flows hydrodynamically, as this damage mechanism has a large effect on which protective measures are feasible with UHPC.

5.3 Fragment containment

To deal with the flying debris created in an explosion, Walker et al. (2011) developed a fragment catcher. The general concept of "catcher" or debris-containment systems is found in several works on blast protection, for example, Webster et al. (2006). A fragment catcher is designed to capture flying debris, whether from the bomb or from other parts of the structure. This is done by using the inertial resistance and strain capacity of the catcher to absorb the kinetic energy of the fragments and transfer the energy to the parts of the structure supporting the catcher. There are two possible uses of UHPC with a catcher system.

1. **Catcher member**. Multiple configurations are possible, including a beam, a steel pipe filled with UHPC (similar to Walker et al. [2011]), a wall, or a panel. Prestressed Ductal® panels, for example, have been tested in fragment simulated projectile (FSP) loading, and found to resist impact energies about twice that anticipated from US 4.2 in. mortar fragments (Cavill et al. 2006). The fragments encountered from a truck bomb or a fragmented structural member are likely larger, but it is possible to scale up the panel design.

2. **Catcher restraint system**. UHPC could be used in columns, not only because of its high compressive strength, but also because of its relatively good tensile strength. This would increase flexural resistance to the lateral loads that would result from fragment impacts on the catcher member. The choice of materials for a catcher system will depend on the specific design used, of course; structural steel is a better choice for members resisting tensile loads. For applications requiring ductility, steel is the conventional choice, although cementitious materials such as UHPCC and ECC are more ductile than conventional concrete, with tensile strain capacities of 0.6% and 5%, respectively.

As Walker et al. (2011) stressed, the catcher requires sufficient restraint to avoid becoming a large damaging fragment.

5.4 Column strengthening

Although Webster et al. (2006) is primarily concerned with retrofitting buildings for blast resistance, some of the ideas presented therein could apply to bridge piers. These concepts apply to both new construction and retrofits. However, retrofits are more difficult to install. The design of stronger columns could use confined UHPC with a steel (or other material) jacket. In the case of a retrofit, the jacket is placed around the existing column and then infilled with UHPC. The jacket provides confinement, which increases the compressive strength of the UHPC, and also causes it to behave in a more ductile manner. Using the UHPC provides additional column capacity and increases mass, giving more inertial resistance to blast effects. It is unreasonable to expect the column to not incur damage after a blast, but the column design could ensure the residual capacity is sufficient to prevent disproportionate collapse. A similar system was also considered by Fujikura et al. (2008) for bridge piers with resistance to either seismic or blast events.

Strengthening of columns could also use unconfined UHPC. Past work on concrete bridges under near-contact or medium standoff blasts indicated

that the main damage mechanisms are cratering, spalling, and breaching (Fujikura et al. 2008). *Cratering* and *spalling* are mass loss on the front and rear faces, respectively. *Breaching* is puncture through the member thickness. A UHPC with high tensile strength, such as CEMTEC$_{multiscale}$®, could be used as a cladding to resist cratering or spalling.

Adding drop panels or column heads made of UHPC with suitable reinforcement detailing could also strengthen the girder-column connection. This is mainly suited to new construction because suitable detailing is difficult to provide in a retrofit. The enhanced connection provides increased resistance to punching shear through the girder near the support (Webster et al. 2006).

5.5   Bridge decks

A blast on the bridge deck would involve near-contact or contact detonation. In this case, the pavement and decking would probably act as a sacrificial shield. If UHPC performs well as a sacrificial shield for near-contact blasts (see Section 5.2), UHPC overlays that are currently considered for durability and bridge rehabilitation (Buitelaar et al. 2004; Denarié et al. 2005; Brühwiler and Denarié 2008; Harris et al. 2011) could also help mitigate blast effects on the girders below. Because the girders and columns are more important structurally, the deck can be considered sacrificial for blasts both below and above the deck (Winget et al. 2005; Kiger et al. 2010). However, losing part of the deck could adversely affect the structural integrity of some bridge types, such as posttensioned segmental box girder bridges. Due to confinement effects and reflections, it is desirable for the deck to allow for venting of a below-deck blast (Winget et al. 2005). Thus, depending on the threats considered for a given bridge, it is important that the deck be strong enough to provide some resistance to above-deck blasts while not being overly strong and trapping blast pressure from below-deck blasts.

6   SDOF Analysis Methodology

6.1   Candidate cementitious materials

Five of the six materials listed in Chapter 2 were examined using a simple
SDOF numerical model. The sixth material, UHPCC, was not included, since
it lacked tensile property data needed for modeling. The candidate materials
and the properties relevant to the model are listed below in Table 30.

Table 30. Selected material properties of candidate materials.

Property	Ductal®	Flexbinder	B5Q (2.5 vol % fibers)	CEMTEC$_{multiscale}$®	SHCC/ECC
Static elastic modulus, E (psi)	7,650,000	9,425,000	8,642,000	7,323,000	2,944,000
Poisson's ratio, ν (–)	0.19	0.2 [1]	0.2 [1]	0.21	0.2 [1]
Dynamic tensile strength, f_{td} (psi)	3,600	2,720	4,490	19,000	1,750
Dynamic compressive strength, f'_{cd} (psi)	26,600	33,900	33,200	32,700	9,700
Unit weight, γ (pcf)	155	175	163	186	119

[1]Generic value used in absence of actual data (AFGC 2013).

All elastic moduli are static values, since dynamic data were scarce; and the
available data showed relatively small variation with strain rate. The tensile
strengths are dynamic values at a strain rate of about 20 s^{-1}. Experimental
data for Ductal®, Flexbinder, and SHCC/ECC (values at strain rates of 19,
~20, and 25 s^{-1}, respectively) were used without modification. The tensile
strength for B5Q was interpolated to 20 s^{-1} using the modified CEB-FIP
equation (Malvar and Ross 1998). The data for CEMTEC$_{multiscale}$® goes up
to only 13.2 s^{-1}; the tensile strength was converted from the modulus of
rupture at this strain rate using a linear correlation as discussed in
Section 4.1. More information on the interpolation and conversion of
dynamic properties can be found in Appendix A.

Compressive strength was also taken at about 20 s^{-1}. The value for Ductal®
was calculated at 20 s^{-1} using the DIF equation proposed by Ngo and others
(Ngo and Mendis 2008; Ngo et al. 2007b). The Flexbinder value was
measured experimentally at about 20 s^{-1}. The compressive strengths for the
remaining three materials were static values with a likely conservative DIF

of 1.1 applied, since no dynamic values were available. The static compressive strength for SHCC/ECC is from Mechtcherine et al. (2012). All properties for Ductal® are taken from Graybeal (2006), the Flexbinder unit weight is from a manufacturer datasheet (Densit ApS, "Flexbinder"), the SHCC/ECC unit weight is from Mechtcherine et al. (2012), the Poisson's ratio for CEMTEC$_{multiscale}$® is from Rossi et al. (2005), and all values not otherwise noted are from Chapters 3 and 4. For several materials, a generic Poisson's ratio of 0.2 (AFGC 2013) is used due to lack of data.

6.2   Plate

The test structure used in the model was an axisymmetric plate, 4 in. thick and 40 in. in diameter, with fixed boundary conditions. The plate had a thickness-to-diameter ratio of 0.1, which allowed the use of classical Kirchhoff plate theory without too much error. The thickness was also chosen to be at least three times the fiber length in any of the mixes. CEMTEC$_{multiscale}$® had the largest fibers. The specific fiber dimensions are part of the proprietary mix design, but they were about 1 in.

If used for physical testing, a square plate (really a slab) would be used instead, since circular forms are very difficult to construct. A circular clamp support fixture would enforce the axisymmetric conditions and fixed boundary. The slab's edge would need extra space for clamping; if 5 in. were given on each side this would result in dimensions of 4 in. thick and 50 in. square for the resulting slab. If made from the densest material in Table 30, CEMTEC$_{multiscale}$®, the slab would weigh about 1,080 lb.

6.3   Equivalent SDOF properties

An SDOF system consisting of a point mass attached to a massless spring with arbitrary resistance $R(x)$ and no damping was used. A simplified view of the plate setup and an SDOF model are shown in Figure 5. Damping was neglected since it has little effect on the maximum deflection. Neglecting damping was also conservative. An equivalent concentrated load was applied to the mass. Load-mass factors and equivalent stiffnesses were found for the SDOF system based on the material properties, the plate geometry, and the assumed deflected shape.

6.3.1   Kirchhoff plate theory

For a plate of thickness t, the equation relating the transverse deflection u under a constant load per unit area w is

$$\nabla^4 u = \frac{w}{D} \tag{10}$$

where ∇^2 is the Laplacian, and the flexural stiffness D is given by

$$D = \frac{Et^3}{12(1 - v^2)}. \tag{11}$$

A solution for an axisymmetric plate of radius R is given in Bauchau and Craig (2009) as

$$u(r) = \frac{wr^4}{64D} + C_1 + C_2 r^2 + C_3 \ln\frac{r}{R} + C_4 r^2 \ln\frac{r}{R}. \tag{12}$$

Deflection at the center, $u(0)$, must be finite, so $C_3 = C_4 = 0$. For clamped edges, boundary conditions are $u(R) = 0$ and $\theta(R) = \frac{du(r)}{dr}\Big|_{r=R} = 0$.
Applying these boundary conditions leads to

$$u(r) = \frac{w}{64D}(r^2 - R^2)^2. \tag{13}$$

Figure 5. Schematics of (*a*) the plate setup and (*b*) the idealized SDOF system. Note that no gravity is acting on the SDOF system.
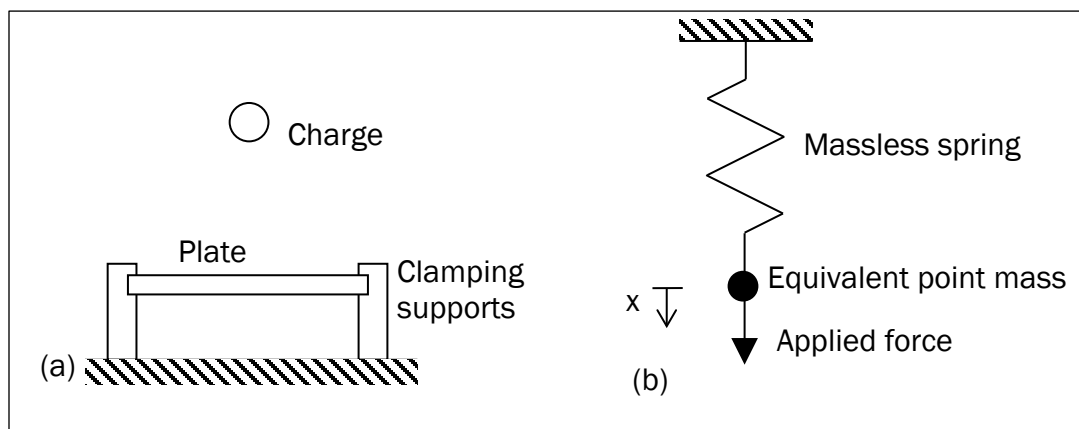
6.3.2 Shape function

For elastic deformations, the deflection of the real plate at a radial distance r from the center and time t is given by $u(r, t) = \phi(r)U(t)$, where the shape function $\phi(r)$ is defined as

$$\phi(r) = \frac{u(r)}{u_{max}} = \frac{u(r)}{u(0)} = \frac{1}{R^4}(r^2 - R^2)^2 \,. \tag{14}$$

Thus, $\phi(r) = 1$ at the point of maximum deflection, which is typically the point of interest for SDOF analysis. The function $U(t)$ is the deflection response of the SDOF equivalent mass over time. The velocity at a point on the real structure is $\dot{u}(r,t) = \phi(r)\dot{U}(t)$, where $\dot{U}(t)$ is the velocity of the SDOF mass.

The first yield in the plate (also referred to as partial failure) is assumed to occur with the formation of a plastic hinge at or near the fixed edge. Following this, the plate is in the elastic-plastic region. A shape function $\phi(r) = 1 - r^2/R^2$ is assumed, satisfying $\phi(0) = 1$ and $\phi(R) = 0$.

The second yield brings the plate into the plastic region. As in Colombo and Martinelli (2011), a conic collapse is assumed with a shape function $\phi(r) = 1 - r/R$.

6.3.3 Load-mass factors

The equivalent mass M is obtained by equating the kinetic energy of the real structure and the mass in the SDOF system (Buchholdt 1997). The real structure has constant mass per unit area $m = \rho t$.

$$\frac{1}{2}M\left(\dot{U}(t)\right)^2 = \frac{1}{2}\int m\left(\dot{u}(r,t)\right)^2 dA,$$

$$\frac{1}{2}M\left(\dot{U}(t)\right)^2 = \frac{1}{2}\int m\left(\phi(r)\dot{U}(t)\right)^2 dA, \text{ and}$$

$$M = \int_0^{2\pi}\int_0^R m(\phi(r))^2 \, r \, dr \, d\theta. \tag{15}$$

The equivalent force $F(t)$ acting on the mass in the SDOF system is found by equating the virtual work done in the SDOF system and the real system (Buchholdt 1997). The force is considered to act through an arbitrary displacement of $U(t)\Delta s$ in the SDOF system and $\phi(r)U(t)\Delta s$ in the real system. The force acting on the real system is a uniform pressure $P(t)$:

$$F(t)(U(t)\Delta s) = \int P(t)(\phi(r)U(t)\Delta s) \ dA,$$

$$F(t) = \int P(t)\phi(r) \ dA, \qquad \text{and}$$

$$F(t) = \int_0^{2\pi} \int_0^R P(t)\phi(r) \ r \ dr \ d\theta. \qquad (16)$$

The load factor K_L is the ratio of the equivalent force to the real force:

$$K_L = \frac{F(t)}{P(t)A}. \qquad (17)$$

The mass factor K_M is the ratio of the equivalent mass to the real mass:

$$K_M = \frac{M}{mA}. \qquad (18)$$

Finally, the load-mass factor is

$$K_{LM} = \frac{K_M}{K_L} = \frac{MP(t)}{mF(t)}. \qquad (19)$$

Applying equations (15), (16), and (19) to the elastic shape function gives

$$M = \frac{m}{R^8} \int_0^{2\pi} \int_0^R r((r^2 - R^2)^2)^2 \ dr \ d\theta = \frac{\pi}{5} mR^2,$$

$$F(t) = \frac{P(t)}{R^4} \int_0^{2\pi} \int_0^R (r^2 - R^2)^2 \ r \ dr \ d\theta = \frac{\pi}{3} P(t)R^2, \text{and}$$

$$K_{LM} = \frac{\left(\frac{\pi}{5} mR^2\right) P(t)}{m \left(\frac{\pi}{3} P(t)R^2\right)} = \frac{3}{5}.$$

The load-mass factors for the elastic-plastic and plastic regions are found in the same way and are given in Table 31.

6.3.4 Equivalent stiffness

The equivalent stiffness K_E of a linear elastic spring in the SDOF system is found by equating the strain energy in the spring and the strain energy in the real system (Buchholdt 1997). Kelly (2013) gives the strain energy in a differential element of an axisymmetric thin plate:

$$\Delta U_s = \frac{D}{2}\left[\left(\frac{\partial^2 u}{\partial r^2} + \frac{1}{r}\frac{\partial u}{\partial r}\right)^2 - 2(1-v)\frac{\partial^2 u}{\partial r^2}\left(\frac{1}{r}\frac{\partial u}{\partial r}\right)\right]\Delta A. \tag{20}$$

Remembering $u = u(r,t) = \phi(t)U(t)$ and substituting the elastic shape function, equation (14), into equation (20), the expression for strain energy becomes

$$\Delta U_s = \frac{D\big(U(t)\big)^2}{2R^8}[(160 + 48v)r^4 + (-128 - 64v)R^2r^2 \tag{21}$$
$$+ (32 + 16v)R^4]\,\Delta A.$$

Equating strain energy in the SDOF ideal spring and the real structure,

$$\frac{1}{2}K_E\big(U(t)\big)^2 = \int dU_s,$$
$$K_E = \frac{D}{R^8}\int_0^{2\pi}\int_0^R [(160 + 48v)r^4 + (-128 - 64v)R^2r^2$$
$$+ (32 + 16v)R^4]\,r\,dr\,d\theta\,,\text{ and}$$
$$K_E = \frac{16\pi Et^3}{9R^2(1-v^2)}. \tag{22}$$

The same approach is followed for the elastic-plastic region. The strain energy simplifies to

$$\Delta U_s = \frac{D\big(U(t)\big)^2}{R^4}(4 + 4v)\Delta A, \tag{23}$$

and the equivalent stiffness is

$$K_E = \frac{D}{R^4}\int_0^{2\pi}\int_0^R (8 + 8v)r\,dr\,d\theta = \frac{2\pi Et^3}{3(1-v)R^2}. \tag{24}$$

Load-mass factors and equivalent elastic stiffnesses are summarized in Table 31. The stiffness in the plastic region is equal to zero assuming perfect plasticity.

Table 31. Load-mass factors and equivalent stiffnesses.

Region	K_{LM}	K_E
Elastic	3/5	$\dfrac{16\pi E t^3}{9R^2(1-v^2)}$
Elastic-plastic	2/3	$\dfrac{2\pi E t^3}{3R^2(1-v)}$
Plastic	1/2	0 (assumed)

6.3.5 Deflection at partial failure

The procedure to find the deflection of the plate's center at partial failure was complex, and the results are somewhat uncertain. The overall approach was to first approximate the state of stress in the plate, convert the stresses to principal stresses, find the load corresponding to the beginning of tensile failure, and then find the deflection at the center of the plate corresponding to that load.

To approximate the stress state, plane stress was assumed. This is a simplifying assumption that allows treating the problem in 2-D, rather than in 3-D, as a proper axisymmetric approach would require. The assumption of plane stress is also used in the development of Kirchhoff plate theory since the effects of shear are ignored (Oñate 2013). For a state of plane stress, the stresses are (Bauchau and Craig 2009)

$$
\begin{bmatrix} \sigma_x \\ \sigma_y \\ \tau_{xy} \end{bmatrix} = \frac{E}{1-v^2} \begin{bmatrix} 1 & v & 0 \\ v & 1 & 0 \\ 0 & 0 & \dfrac{1-v}{2} \end{bmatrix} \begin{bmatrix} \varepsilon_x \\ \varepsilon_y \\ \gamma_{xy} \end{bmatrix}.
\tag{25}
$$

The strains are defined as given below. Simplifying, only the effects of curvature from bending (i.e., only the second derivatives of u) are considered.

$$
\begin{aligned}
\varepsilon_x &= \frac{\partial u_x}{\partial x} - z\frac{\partial^2 u_z}{\partial x^2} \approx -z\frac{\partial^2 u}{\partial x^2} = -\frac{wz}{16D}(3x^2 + y^2 - R^2), \\
\varepsilon_y &= \frac{\partial u_y}{\partial y} - z\frac{\partial^2 u_z}{\partial y^2} \approx -z\frac{\partial^2 u}{\partial y^2} = -\frac{wz}{16D}(x^2 + 3y^2 - R^2), \text{ and} \\
\gamma_{xy} &= \frac{\partial u_x}{\partial y} + \frac{\partial u_y}{\partial x} - 2z\frac{\partial^2 u_z}{\partial x\partial y} \approx -2z\frac{\partial^2 u}{\partial x\partial y} = -\frac{wxyz}{4D}.
\end{aligned}
\tag{26}
$$

An orthogonal coordinate system is used to facilitate computation of principal stresses. Plugging equation (26) into equation (25),

$$
\begin{aligned}
\sigma_x &= \frac{E}{1 - v^2}\left[\varepsilon_x + v\varepsilon_y\right] \\
&= -\frac{3wz}{4t^3}[x^2(3 + v) + y^2(1 + 3v) + R^2(-1 - v)],
\end{aligned}
\tag{27}
$$

$$
\begin{aligned}
\sigma_y &= \frac{E}{1 - v^2}\left[v\varepsilon_x + \varepsilon_y\right] \\
&= -\frac{3wz}{4t^3}[x^2(1 + 3v) + y^2(3 + v) + R^2(-1 - v)], \text{ and}
\end{aligned}
\tag{28}
$$

$$
\begin{aligned}
\tau_{xy} &= \frac{E}{1 - v^2}\frac{1 - v}{2}\gamma_{xy} \\
&= -\frac{3wxyz(1 - v)}{2t^3}.
\end{aligned}
\tag{29}
$$

The Mohr-Coulomb failure criterion was used, since it is relatively accurate for brittle materials, such as concrete. The Mohr-Coulomb failure criterion accounts for both normal and shear stresses. The approach followed here includes only the in-plane shear stress τ_{xy}. The through-plane shear stresses, τ_{xz} and τ_{yz}, are ignored, following Kirchhoff's assumptions. For an element in plane stress, the Mohr-Coulomb failure criterion (Budynas 1999) is

$$
\begin{aligned}
&\text{Case 1: } \sigma_{p1} \leq f_t, && \sigma_{p1} \geq \sigma_{p2} \geq 0, \\
&\text{Case 2: } \frac{\sigma_{p1}}{f_t} - \frac{\sigma_{p2}}{f_c'} \leq 1, && \sigma_{p1} \geq 0 \geq \sigma_{p2}, \text{ or} \\
&\text{Case 3: } |\sigma_{p2}| \leq f_c', && 0 \geq \sigma_{p1} \geq \sigma_{p2}.
\end{aligned}
\tag{30}
$$

For plane stress, the principal stresses σ_{p1} and σ_{p2} are

$$
\sigma_{p1} = \frac{\sigma_x + \sigma_y}{2} + \sqrt{\left(\frac{\sigma_x - \sigma_y}{2}\right)^2 + \tau_{xy}^2} \text{ and}
\tag{31}
$$

$$
\sigma_{p2} = \frac{\sigma_x + \sigma_y}{2} - \sqrt{\left(\frac{\sigma_x - \sigma_y}{2}\right)^2 + \tau_{xy}^2}.
\tag{32}
$$

Substituting the stresses from equations (27)-(29) into equations (31) and (32) and simplifying gives the following results for principal stresses, which are only approximations due to the number of simplifications used in their derivation:

$$\sigma_{p1} = \frac{3wz}{4t^3}[R^2(1+v) - (x^2+y^2)(1+3v)] \text{ and} \tag{33}$$

$$\sigma_{p2} = \frac{3wz}{4t^3}[R^2(1+v) - (x^2+y^2)(3+v)] \ . \tag{34}$$

To find the deflection at partial failure, one can determine the lowest load w_{crit} causing failure at any point and find the deflection corresponding to w_{crit}. Now, the three cases of the Mohr-Coulomb criterion are defined by inequalities in σ_{p1} and σ_{p2}; to find w_{crit}, it is more useful to rewrite them in terms of $r = \sqrt{x^2+y^2}$ and z. First, the relation $\sigma_{p1} \geq \sigma_{p2}$ should hold by definition. Using equations (33) and (34), it is seen to hold for $v \leq 1$. All real materials have $v \leq 0.5$.

Case 1: $\sigma_{p1} \geq \sigma_{p2}$ is always satisfied, and $\sigma_{p2} \geq 0$ reduces to

$$r \leq R\sqrt{\frac{1+v}{3+v}} \quad \text{and} \quad z \geq 0$$

$$\text{or} \quad r \geq R\sqrt{\frac{1+v}{3+v}} \quad \text{and} \quad z \leq 0. \tag{35}$$

At the onset of failure,

$$\sigma_{p1} = \frac{3w_{crit,1}z}{4t^3}[R^2(1+v) - r^2(1+3v)] = f_{td}. \tag{36}$$

The smallest value of $w_{crit,1}$ subject to the constraints of equation (35) occurs for $z = t/2$ and $r = 0$:

$$w_{crit,1} = \frac{8f_{td}t^2}{3R^2(1+v)}. \tag{37}$$

Case 2: The intersection of $\sigma_{p1} \geq 0$ and $\sigma_{p2} \leq 0$ reduces to

$$R\sqrt{\frac{1+v}{3+v}} \le r \le R\sqrt{\frac{1+v}{1+3v}} \quad \text{and} \quad z \ge 0$$

$$\text{or} \quad \left(r \ge R\sqrt{\frac{1+v}{1+3v}} \text{ or } r \le R\sqrt{\frac{1+v}{3+v}} \right) \quad \text{and} \quad z \le 0. \tag{38}$$

At the onset of failure,

$$\frac{\sigma_{p1}}{f_{td}} - \frac{\sigma_{p2}}{f'_{cd}} = \frac{3w_{crit,2}z}{4f_{td}t^3}[R^2(1+v) - r^2(1+3v)]$$

$$- \frac{3w_{crit,2}z}{4f'_{cd}t^3}[R^2(1+v) - r^2(3+v)] = 1 \ . \tag{39}$$

The smallest $w_{crit,2}$ that satisfies the constraints of equation (38) is dependent on the material's tensile and compressive strengths, and is given by

$$w_{crit,2} = \min\left[\frac{4f_{td}t^2}{3R^2\left(v - \frac{f_{td}}{f'_{cd}}\right)}, \frac{4(1+3v)f_{td}t^2}{3R^2(1-v^2)} \right], \tag{40}$$

where the arguments correspond to failure at $z = -t/2, r = R$ and $z = t/2$, $r = R\sqrt{(1+v)/(1+3v)}$, respectively.

Case 3: $\sigma_{p1} \ge \sigma_{p2}$ is always satisfied, and $\sigma_{p1} \le 0$ reduces to

$$r \geq R \sqrt{\frac{1+v}{1+3v}} \quad \text{and} \quad z \geq 0$$

$$\text{or} \quad r \leq R \sqrt{\frac{1+v}{1+3v}} \quad \text{and} \quad z \leq 0. \tag{41}$$

At the onset of failure,

$$|\sigma_{p2}| = f'_{cd}$$

$$-\sigma_{p2} = \frac{3w_{crit,3}z}{4t^3}[-R^2(1+v) + r^2(3+v)] = f'_{cd}, \tag{42}$$

since $\sigma_{p2} \leq 0$. The smallest value of $w_{crit,3}$ subject to the constraints of equation (41) occurs for $z = t/2$ and $r = R$.

$$w_{crit,3} = \frac{4f'_{cd}t^2}{3R^2}. \tag{43}$$

The value of w_{crit} is then the smallest of the $w_{crit,i}$values.

$$w_{crit} = \min\left[\frac{8f_{td}t^2}{3R^2(1+v)}, \frac{4f_{td}t^2}{3R^2\left(v - \frac{f_{td}}{f'_{cd}}\right)}, \frac{4(1+3v)f_{td}t^2}{3R^2(1-v^2)}, \frac{4f'_{cd}t^2}{3R^2}\right]. \tag{44}$$

Evaluating equation (44) for each of the candidate materials shows that the third expression is the minimum value. It corresponds to case 2 and failure at $z = t/2, r = R\sqrt{(1+v)/(1+3v)} \approx 0.87R$.

Finally, the approximate deflection at the center of the plate at partial failure is

$$u(0) = \frac{3(1-v^2)w_{crit}R^4}{16Et^3} = \frac{1+3v}{4}\left(\frac{f_{td}}{E}\right)\left(\frac{R^2}{t}\right) = x_{el}. \tag{45}$$

The deflection at the center of the plate that occurs at the second yield may be crudely approximated by applying the failure criterion developed above to the center of the plate. The deflection function used was that for the elastic region, so applying it to the elastic-plastic region will involve some error. On the other hand, the plastic hinges form near the edges initially and should not affect the overall response shape in the center too much. The center deflection is greater, but that is difficult to quantify.

Failure in the center is covered by case 1 of the Mohr-Coulomb failure criterion, with critical load $w_{crit,1}$ as given by equation (37). The deflection at the center of the plate when failure occurs in the center is about

$$u(0) = \frac{1-\nu}{2}\left(\frac{f_{td}}{E}\right)\left(\frac{R^2}{t}\right) = x_{pl}. \tag{46}$$

This is only a crude approximation, since the elastic deflection function was applied to the elastic-plastic region, but it should suffice for the purposes of an SDOF analysis. For the materials considered, calculations show that the deflection at second yield x_{pl} is at most 0.0006 in. greater than the deflection at first yield x_{el}. Because of this and the uncertainty in the behavior of the plates after partial failure, a one-step resistance function with constant resistance after reaching x_{el} is used.

6.3.6 Resistance function

The one-step elastic-plastic resistance function from UFC 3-340-02 (USACE 2008) was used. This function has the form

$$R(x) = \begin{cases} K_E x, & x < x_{el} \\ R_u, & x \geq x_{el} \end{cases}, \tag{47}$$

where $R_u = K_E x_{el}$. A more complex resistance function should be based on experimental data on the behavior of these UHPCs.

Although stiffness and load-mass factors were calculated for elastic, elastic-plastic, and plastic behavior, the results of the previous section show that it is acceptable to neglect the behavior of the elastic-plastic region for the plate. Instead of an SDOF analysis, a more detailed analysis is appropriate for the inclusion of the elastic-plastic behavior. Such an analysis could model the elastic-plastic region more accurately.

The resistance function parameters for all five UHPCs are listed in Table 32.

Table 32. Elastic-plastic resistance function parameters.

Property	Ductal®	Flexbinder	B5Q (2.5 Vol % Fibers)	CEMTEC$_{multiscale}$®	SHCC/ECC
K_E (lbf/in.)	7,092,132	8,773,188	8,044,339	6,845,795	2,740,400
x_{el} (in.)	0.0185	0.0115	0.0208	0.1057	0.0238
R_u (lbf)	130,996	101,276	167,179	723,796	65,159

6.4   Blast loading

Values of reflected pressure and reflected impulse for the simulated blasts were taken from the 'spaghetti charts' in UFC 3-340-02 (USACE 2008). The various blast load cases are listed in Table 33. Case 1 is intended to cause minimal plastic deformation with mostly elastic or elastic-plastic behavior. Case 2 is intended to cause significant plastic deformation. Cases 3a and 3b are both intended to cause failure, although only case 3b may cause failure for some materials. A standoff of 48 in. is used for all blasts.

Table 33. Blast load cases.

Load case	Charge Weight, W (lbs TNT)	Standoff, R (in.)	Scaled Range, Z (ft/lb$^{1/3}$)	Predicted Peak Pressure, P (psi)	Predicted Peak Impulse, i (psi-ms)	Equivalent Duration, t_{of} (ms)
1	2	48	3.17	380	60.5	0.318
2	5	48	2.34	900	120	0.266
3a	16	48	1.59	2400	277	0.231
3b	24	48	1.39	3200	404	0.252

In the SDOF model, the load from the blast is modeled as a triangular pulse with zero rise time and the same peak pressure, P, as the real blast. The equivalent (or fictitious) duration t_{of} preserves the total impulse, i, of the blast:

$$t_{of} = \frac{2i}{P}. \tag{48}$$

The pressure from the triangular pulse is

$$P(t) = \begin{cases} P\left(1 - \dfrac{t}{t_{of}}\right), & t \leq t_{of} \\ 0, & t > t_{of}. \end{cases} \tag{49}$$

6.5   Numerical integration

Two methods of numerical integration, the predictor-corrector average acceleration and acceleration impulse extrapolation methods, were used to solve the equation of motion for the SDOF system. The equation of motion is given by equation (50),

$$K_{LM} m_{plate} \ddot{x}(t) + R\big(x(t)\big) = P(t)A, \tag{50}$$

where K_{LM} is the load-mass factor given by equation (19); m_{plate} is the mass of the real plate, lbf·s²/in.; $x(t)$ and $\ddot{x}(t)$ are the position and acceleration of the point mass, in. and in./s², respectively; $R(x)$ is defined by equation (47), lbf; $P(t)$ is the triangular pressure pulse from equation (49), psi; and A is the area of the circular plate, in.² A load-mass factor of 0.60 is used for blast case 1 (see Section 6.3.3), where mainly elastic behavior is expected, with 0.50 being used for all other blast cases, where significant plastic deformation is expected.

The procedures for both methods are found in UFC 3-340-02 (USACE 2008). The algorithms were implemented in Microsoft Excel, and a time-step of 5 μs was used.

6.6   Interpretation of results

The behavior of the SDOF models for each material was calculated for all four blast loads using both solution methods. This resulted in 40 simulations. For convenience, an abbreviated ID is used to refer to the simulation runs. The naming scheme is shown in Figure 6. For example, D-1-P refers to the simulation for Ductal® under blast case 1, minimal damage, using the predictor-corrector average acceleration method.

Figure 6. Simulation naming scheme.

First letter of material	-	Blast case	-	First letter of solution method
B5Q		1		Acceleration impulse extrapolation
CEMTEC_{multiscale}®		2		Predictor-corrector average acceleration
Ductal®		3a		
Flexbinder		3b		
SHCC/ECC				

The SDOF model output consisted of the time-deflection history of the center of the plate. For a comparison between the different materials, only the maximum deflection and the time at which it occurred were used. The maximum deflection, x_m, was also used to calculate the ductility ratio, $\mu = x_m/x_{el}$, and the support rotation, $\Theta = \text{atan } 2x_m/L = \text{atan } x_m/R$.

According to UFC 3-340-02 (USACE 2008), conventional reinforced concrete fails at a support rotation of about 6°. Members with laced reinforcement may sustain up to 12° support rotation before loss of integrity. Newmark (1953) suggests that the maximum ductility ratio for a

moderately ductile structure is $\mu = 30$. Williamson et al. (2010) quotes typical failure criteria for slabs in bending in terms of x_m/L: the deflection ratios corresponding to light, moderate, and severe damage are 4%, 8%, and 15%, respectively. These are suggested failure criteria and may not apply well to the materials tested in the simulation. However, the suggested failure criteria provide a reasonable approximation of the behavior limits for plates subjected to blasts.

7   SDOF Results

The compiled results from all simulations are found in Appendix B. The difference between the two integration methods used is quite small (see Section 7.2), so results from the predictor-correct average acceleration method are used for the comparison graphs in this section.

Figure 7 compares the maximum deflection for each material at the four levels of blast load considered in the numerical simulation. The blast intensity is expressed in terms of the peak impulse. Because the pressure subsides so quickly, it has little effect on the structure compared to the impulse, which determines the energy imparted to the structure. The deflection increases nonlinearly as the peak impulse increases. The relative performance of each material does not change at different impulses, which is likely due to the way DIFs were handled. Calculating an instantaneous strain rate in the material is difficult due to plasticity, so the tensile and compressive strengths were taken at a strain rate of about 20 s^{-1} for all materials. A more accurate approach would have used differing strain rates for each blast scenario, which may show further differences in the behavior of each material.

Figure 7. Comparison of maximum deflection for each material.
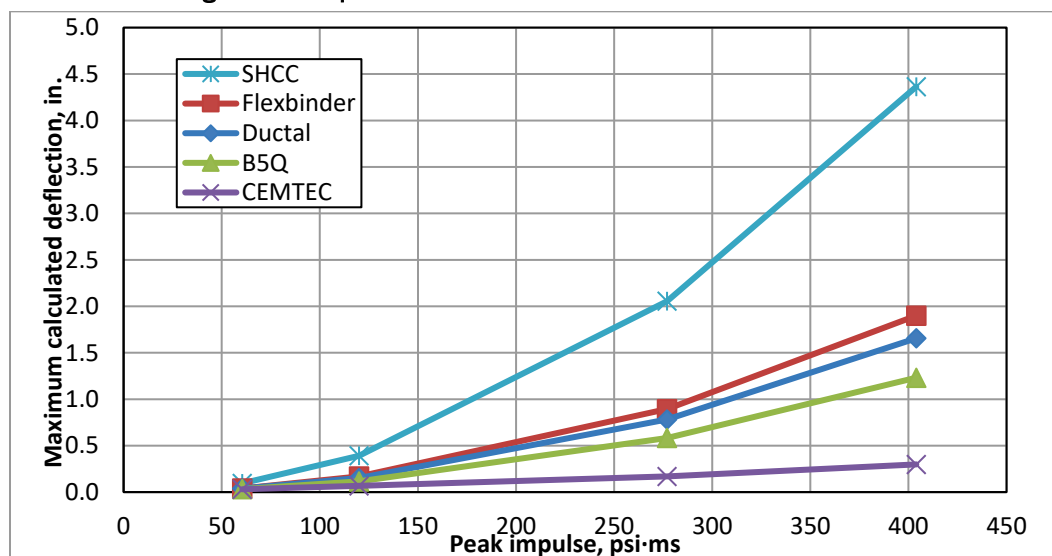
The differences in maximum deflection between materials were relatively small for load case 1. The differences were more significant for load case 2, although four of the materials behaved very similarly. At the highest peak impulse, load case 3b, the lowest deflection was about 0.3 in., for

CEMTEC$_{multiscale}$®. At the other extreme, results show SHCC/ECC deflecting almost 4.5 in. Flexbinder, Ductal®, and B5Q behavior ranged in between the extremes with maximum deflections of 1 to 2 in.

Figure 8 compares the ductility ratio μ for each material at the four blast levels considered in the simulation. The same relative order of material behaviors is seen in Figure 7. The materials can be divided into three groups: those with a high μ, SHCC/ECC and Flexbinder; those with a moderately high μ, Ductal® and B5Q; and those with a low μ, CEMTEC$_{multiscale}$®. The ductility ratio expresses deflection in terms of the maximum elastic deflection (i.e., deflection at partial failure) x_{el}. Therefore, CEMTEC$_{multiscale}$®, which had the lowest maximum deflection in the simulation as well as the highest x_{el}, has a far lower μ than any of the others. Flexbinder has the lowest x_{el}, which increases its μ much more than those of Ductal® and B5Q, giving it the second-highest μ. SHCC/ECC has the second-highest x_{el} as well as a very large deflection due to its low stiffness, giving it the highest μ.

Figure 8. Comparison of maximum ductility ratio for each material.
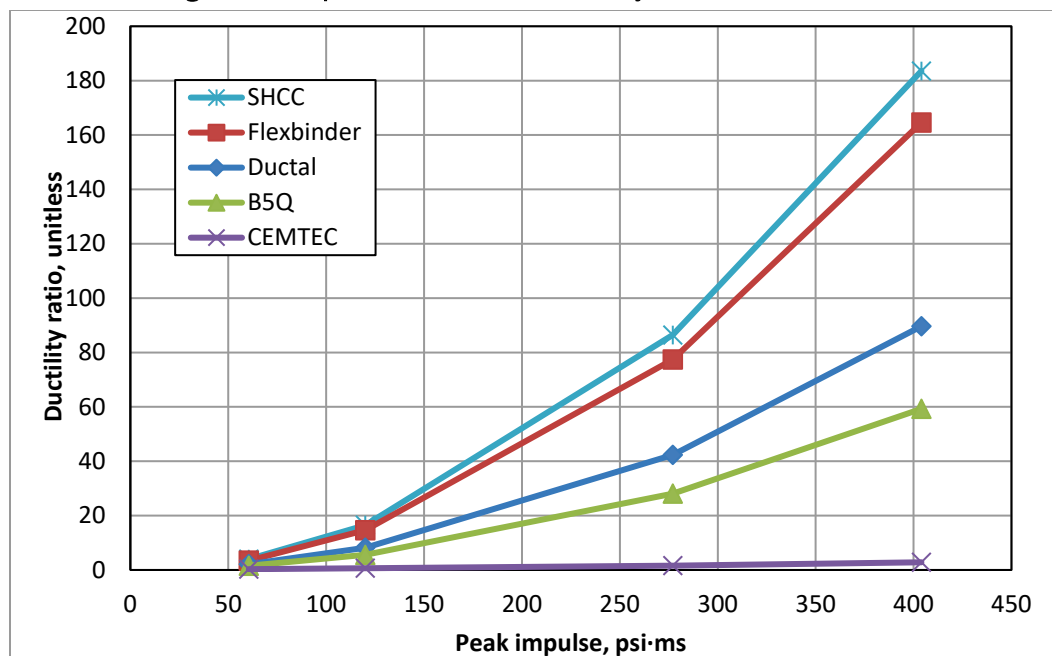
7.1 Relationship between deflection and material properties

Many factors affect the deflection of the plate using the SDOF model: the mass, the equivalent stiffness, the deflection at yield, and the ultimate resistance (which is a function of the stiffness and deflection at yield). These model properties are calculated from the physical and mechanical

properties of the materials, the density, tensile strength, elastic modulus, and Poisson's ratio. To examine the effect of the material properties on performance, the maximum deflection was plotted against eight physical, mechanical, and model properties and analyzed for trends. The deflection results are from load case 3*b*, using the predictor-corrector average acceleration method. Using the data from one case gives only five data points, and the following is not a rigorous analysis nor is it applicable to UHPCs in general. Also, examining correlation one variable at a time will not bring out the (likely complex) relationship among all the variables.

Figure 9 shows maximum deflection versus unit weight. Since the plate geometry was held constant, materials with a higher unit weight have higher inertial resistance. Thus, it is expected that deflection should decrease with increasing unit weight, as the figure shows. The linear regression fit (coefficient of determination $r^2 = 0.86$) is only moderately good, considering how few data points there are. Other properties also have a strong influence on the deflection.
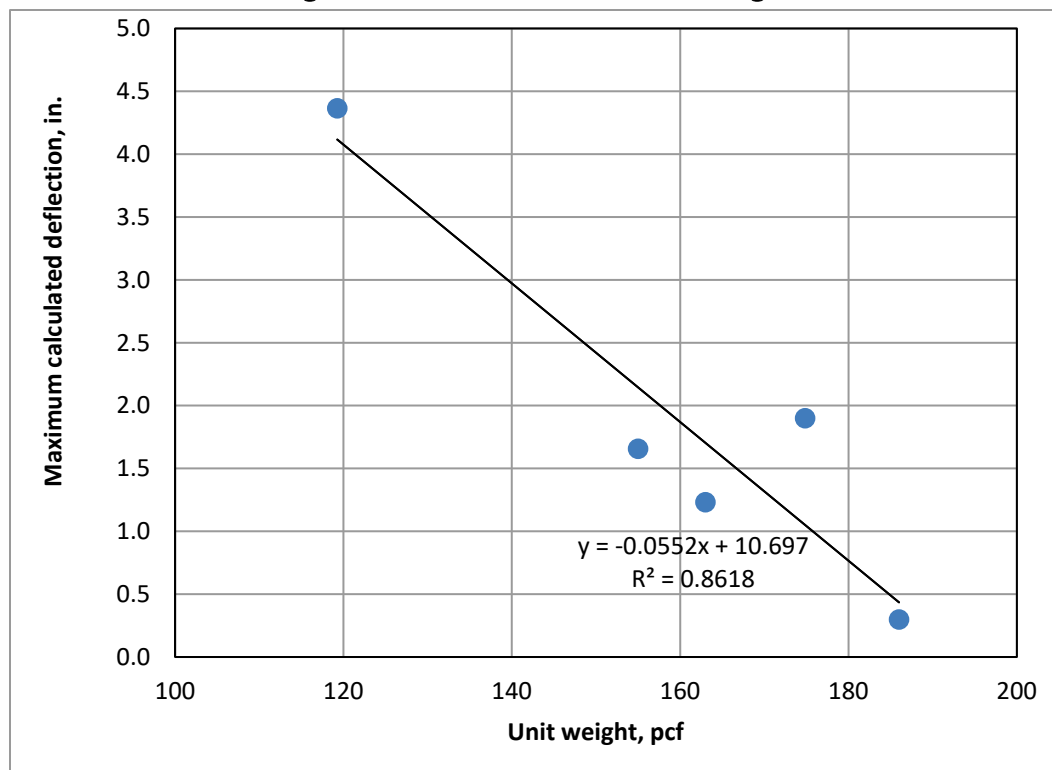
Figure 9. Maximum deflection vs. unit weight.

$$y = -0.0552x + 10.697$$
$$R^2 = 0.8618$$

Figure 10 shows maximum deflection versus Poisson's ratio, ν. Three of the five materials have the same (assumed) ν, and the data for these three

materials show that other factors besides v have a large effect on the maximum deflection. Regardless, v varies only from 0.19 to 0.21, which is quite small compared to the variation in other properties, so its effect on deflection should be proportionally small as well.

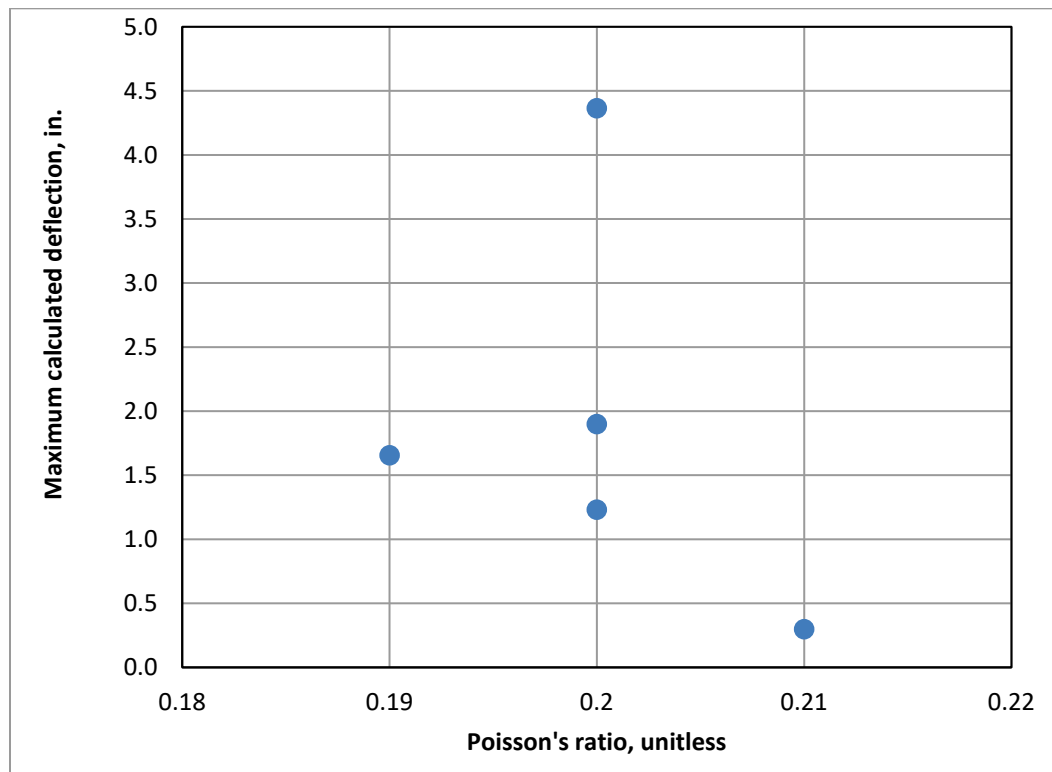Figure 10. Maximum deflection vs. Poisson's ratio.

Figure 11 shows maximum deflection versus tensile strength. A strong correlation appears to exist between the two; the power function fit has a coefficient of determination $r^2 = 0.98$. The relationship resembles an inverse proportion, with an exponent of -1.072. A similar relationship is seen in Figure 12, which depicts maximum deflection as a function of ultimate resistance. These data follow a power function with an exponent of -1.059 ($r^2 = 0.98$). The only significant difference between the two equations is the multiplicative constant. Intuitively, this makes sense, as the ultimate resistance is essentially the geometry-specific analog of the ultimate tensile strength.

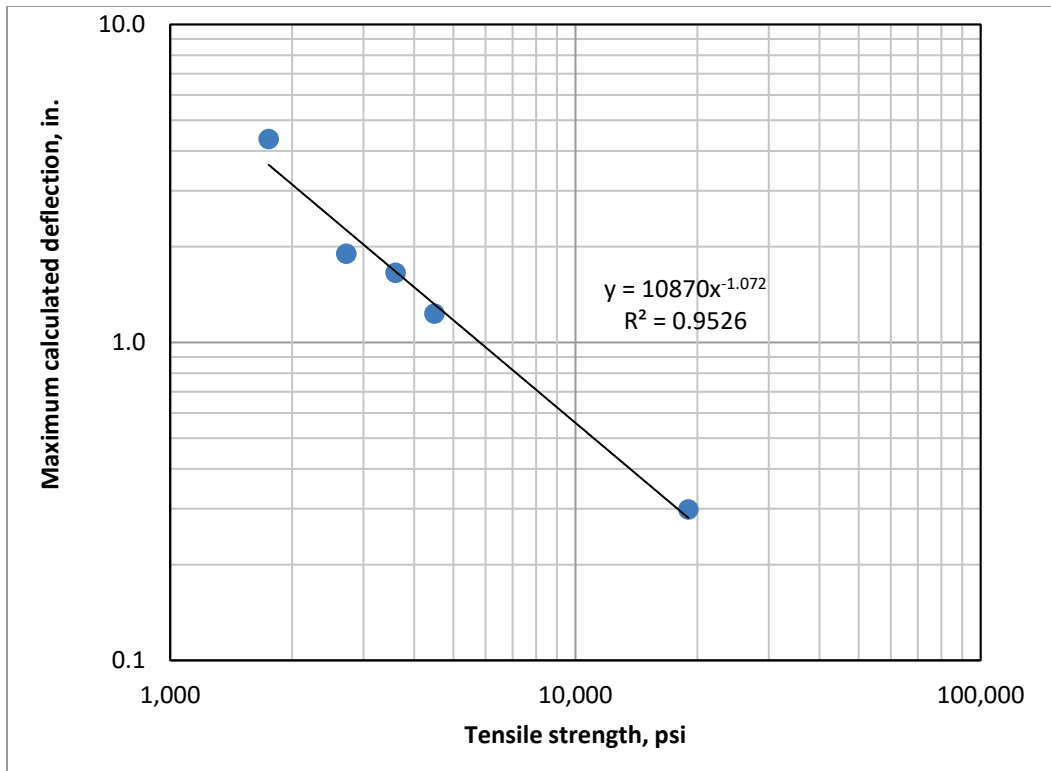Figure 11. Maximum deflection vs. tensile strength.

$y = 10870x^{-1.072}$
$R^2 = 0.9526$

Figure 12. Maximum deflection vs. ultimate resistance.
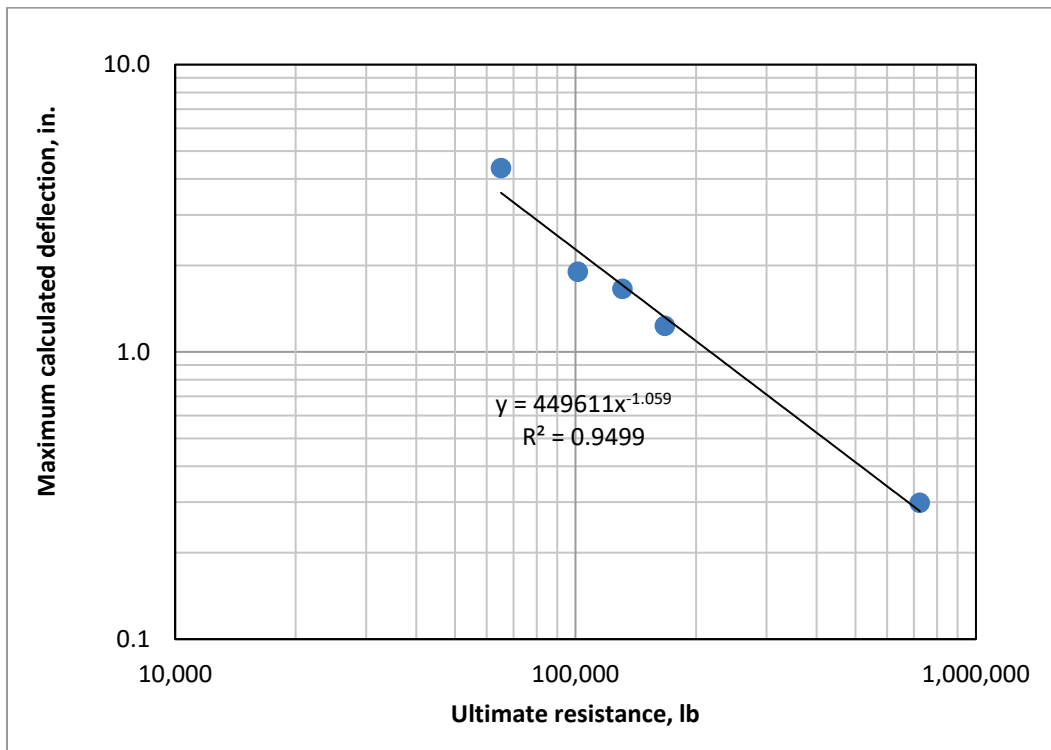

$y = 449611x^{-1.059}$
$R^2 = 0.9499$

Figure 13 shows maximum deflection versus elastic modulus. No particularly strong correlation appears, perhaps because most of the response results from plastic deformation. Figure 14 shows maximum deflection versus the equivalent stiffness, which is the geometry-specific analog of the elastic modulus. The same overall scatter of data is seen, with some slight differences due to differing Poisson's ratios. This is expected, because the equivalent stiffness is a function of the elastic modulus.

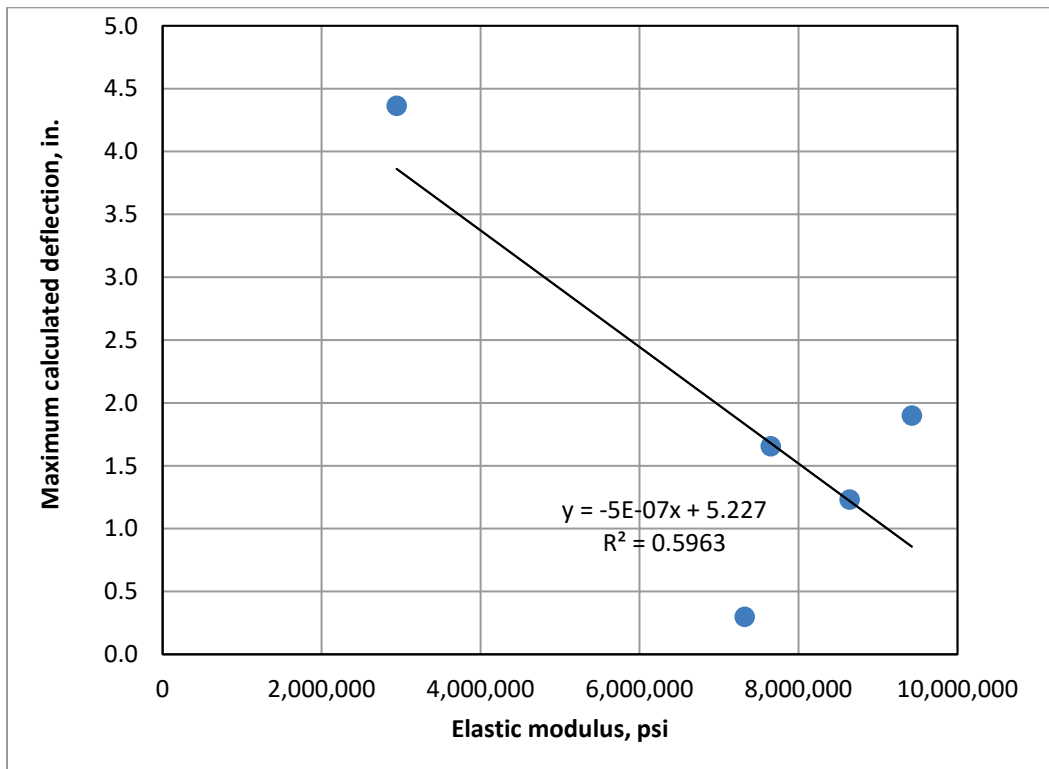Figure 13. Maximum deflection vs. elastic modulus.

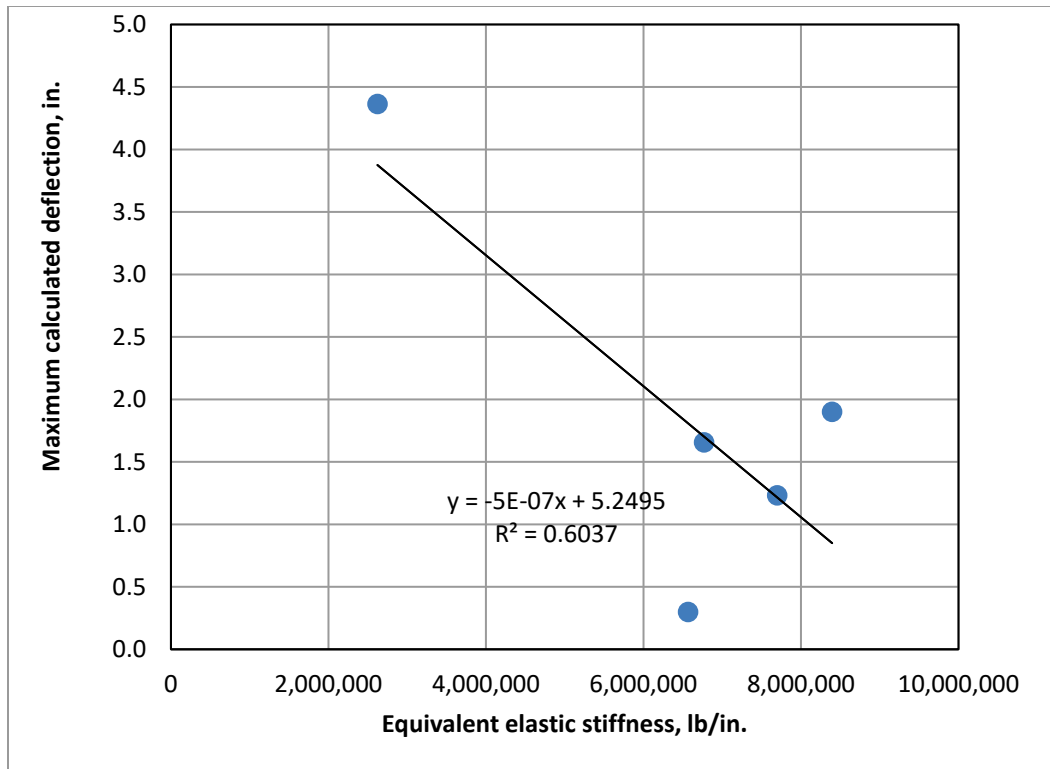Figure 14. Maximum deflection vs. equivalent stiffness.

Figure 15 shows maximum deflection versus the ratio of tensile strength to elastic modulus, f_{td}/E. From equation (47), if plate geometry is constant, and Poisson's ratio is assumed constant as well (v differs little between the five materials), the deflection at first yield is proportional to f_{td}/E. Thus, Figure 16, a plot of maximum deflection versus deflection at yield, shows essentially the same scatter of data as Figure 15. The best fit was given by an exponential function, although the correlation is only moderately good, with $r^2 = 0.72$ for both.

Figure 15. Maximum deflection vs. ratio of tensile strength to elastic modulus.
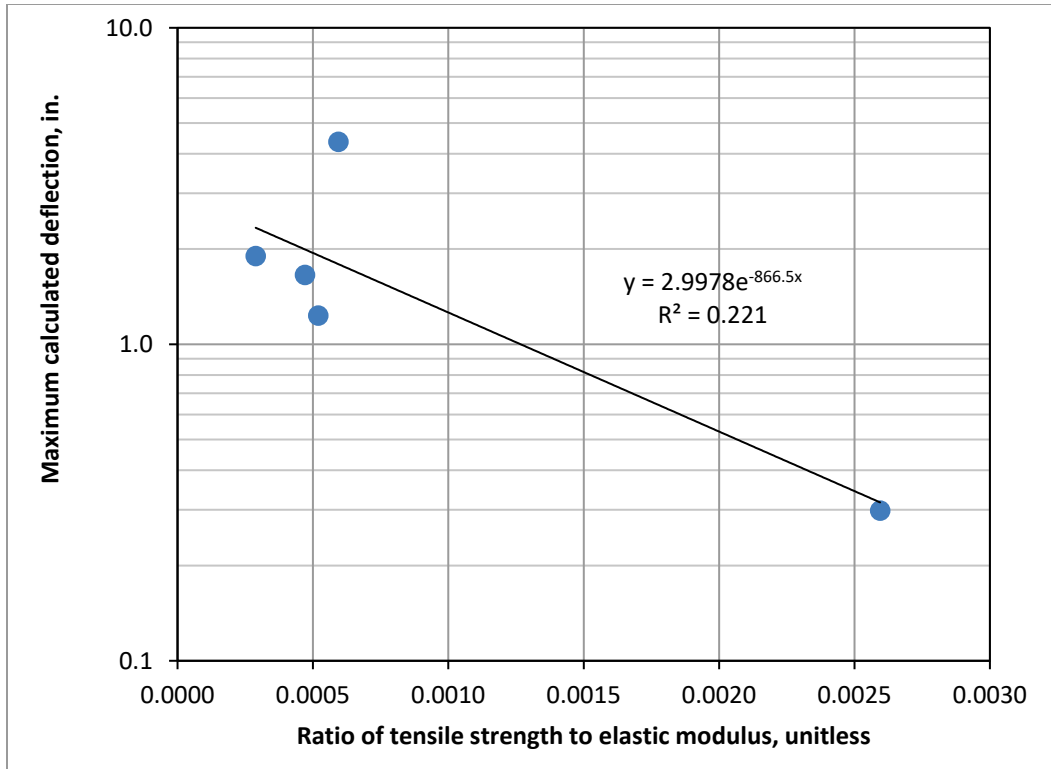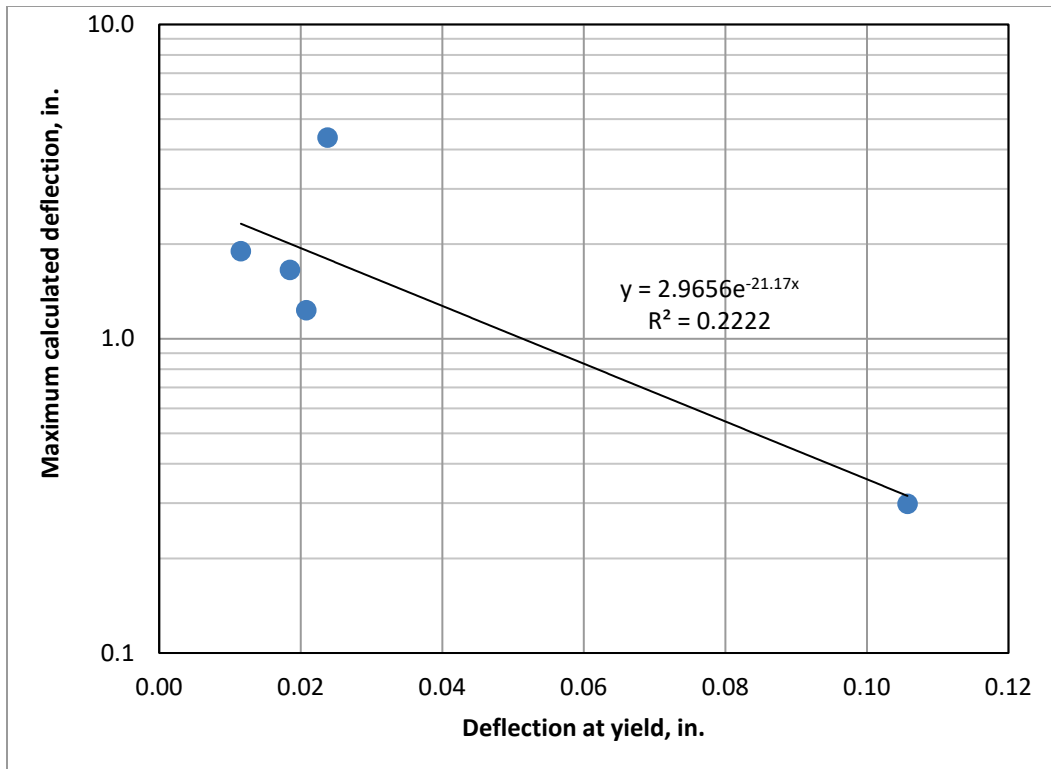

Figure 16. Maximum deflection vs. deflection at yield.

7.2 Method comparison

Figure 17 compares the differences between the two integration methods for three selected cases: C-3b-A/P, D-2-A/P, and F-1-A/P. The differences here are quite small, on the order of 10^{-5} in. In all the data (see Appendix B), the largest difference between the two methods occurs for B5Q in load case 3*b* and Flexbinder in case 3*a*, where the values differ by about 10^{-4} in. In several cases, the acceleration impulse method has the maximum deflection occurring 1 time-step, 5 μs, later than it does with the predictor-corrector average acceleration method. Note that Figure 17 is not a straight-line plot of a few data points; the difference was calculated at each of 300−450 data points on the response curve (the number depends on the case chosen). Remarkably, the error between the two methods follows a piece-wise linear relationship over time. As the events marked on the graph indicate, the transitions between linear segments seem to correspond to sudden changes in either the applied force or the resisting force. The maximum deflection is also marked on the plot, but it does not have any special significance, apart from falling approximately in the middle of one of the descending segments.

Figure 17. Comparison of difference between the acceleration-impulse extrapolation and predictor-corrector average acceleration methods over one half-cycle of response. Pertinent events are marked as shown in the legend.
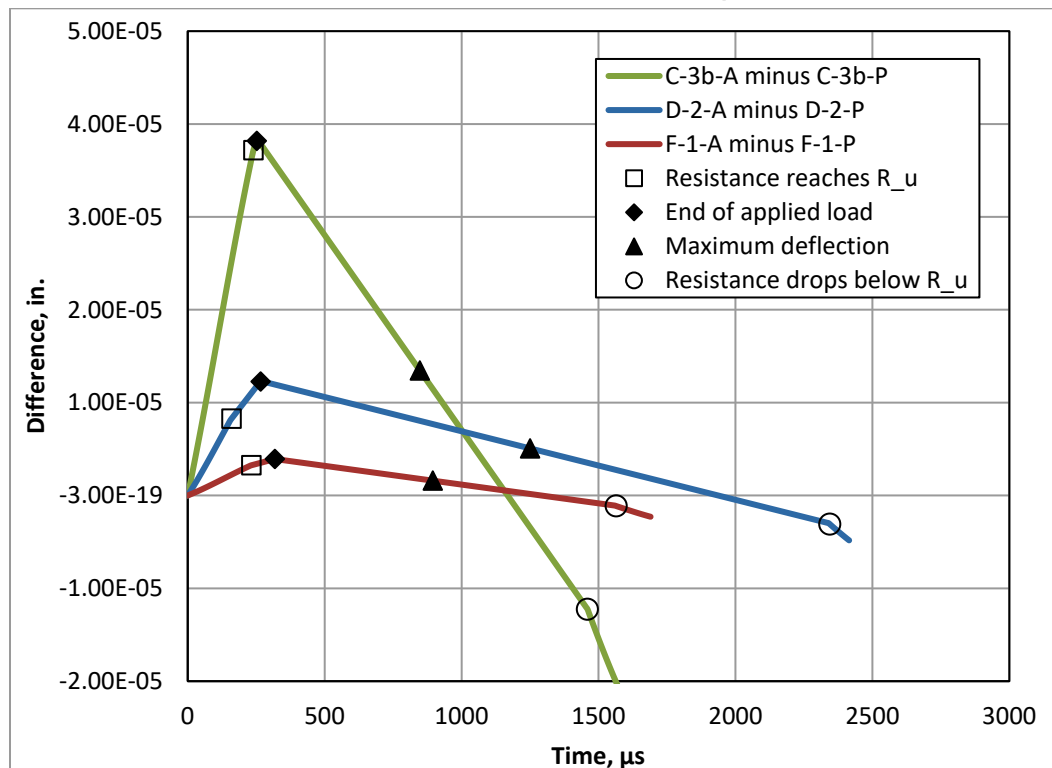
8   Conclusions

8.1   Material property literature search

1. If high tensile strength is desired, CEMTEC$_{multiscale}$® and B5Q appear to be the best choices.
2. Densit® Flexbinder provides the best compressive strength of the UHPCs considered.
3. If Densit® products are chosen, tests should be conducted to compare Inducast TT5 and Flexbinder, as Inducast TT5 will likely provide superior performance despite a scarcity of test data.
4. Fracture performance was characterized using many different properties, which, along with sparse data, made comparison between the UHPCs difficult.
5. For applications in which stiffness is important, Densit® Flexbinder had the highest elastic modulus in static conditions, but no data were available for dynamic conditions. B5Q had the best performance of the UHPCs with dynamic data available.
6. Tests should be conducted to determine under which blast conditions the chosen UHPC flows hydrodynamically, as this damage mechanism has a large effect on which protective measures are feasible with the UHPC.
7. Ductal® has been used in several studies on blast and fragment impact resistance. Similar studies were more difficult to find for other UHPCs. While some indirect comparisons are possible based on material properties, the blast protection performance of the various UHPCs are best compared through testing. This is another area for future work, depending on available funding and material choice.
8. UHPC could be used for blast-resistant columns, either with or without confinement from a steel (or similar) jacket. UHPC could also be used to strengthen column-girder connections against shear by using drop panels or column heads, if the necessary reinforcement detailing is provided.
9. UHPC could be used in a fragment catcher system, either as part of the catcher member (beam, panel, etc.) or as part of the restraint system.
10. Depending on the results of item 6, UHPC overlays for bridge durability or rehabilitation may also be able to serve as sacrificial shields if hydrodynamic flow of the UHPC is not a significant risk. The specific design will depend on whether blasts are anticipated to occur above deck, below deck, or both. For above-deck blasts, the deck can be used as a sacrificial shield; for below-deck blasts, the deck should be designed to allow pressure venting.

8.2 SDOF analysis

1. The CEMTEC_{multiscale}® plate deflected least in the simulations, with a maximum deflection of about 0.3 in. under the largest blast load. Ductal®, the most commonly available commercial UHPC in North America, deflected almost 5.5 times as much as CEMTEC_{multiscale}®, and fell in the middle of the five materials tested. SHCC/ECC had the largest deflection, about 14.5 times that of CEMTEC_{multiscale}®.

2. Based on regression analysis of results from the SDOF model, the ultimate tensile strength appeared to have the greatest effect on the maximum deflection of the UHPC plates. Inertial resistance also played a large role, and maximum deflection also decreased with increasing unit weight, since plate geometry was constant. The correlation was only moderately strong. The elastic modulus also had a moderate effect on the maximum deflection, though not as great as might have been expected. This may be because of the large role plastic deformations play.

3. Using numerical integration in Microsoft Excel worked well for studying simple SDOF models. With a time-step of 5 μs, there was no appreciable difference between the two integration methods used, and 2,900 time-steps could be run in less than a second on a PC.

4. It is important to remember that all results from the SDOF model are heavily influenced by the assumptions and simplifications made. The formulation of the resistance function used many simplifications, particularly regarding deflection at partial failure, and only bending effects were considered.

5. Future work can also incorporate dynamic increase factors (DIFs) more robustly. Here, the DIF for each material was set using one strain rate. The strain rate was assumed to be the same for all four blast scenarios, an unrealistic assumption. A better approach would be determining an approximate or average strain rate for the material in each of the blast scenarios and basing the DIFs on that. This is difficult to do, however, because of the plastic deformations in the material. Calculating strain rates in the material at each time-step and adjusting material properties would be more realistic, but likely beyond the scope of an SDOF model.

References

ACI Committee 239. 2018. *Ultra-high-performance concrete: an emerging technology report*. ACI 329-18R. Farmington Hills, MI: American Concrete Institute.

ACI Committee 318. 2011. *Building code requirements for structural concrete*. ACI 318-11 and commentary. Farmington Hills, MI: American Concrete Institute.

AFGC. 2013. *Ultra high performance fibre-reinforced [sic]: Recommendations* [Bétons Fibres á Ultra-Hautes Performances: Recommandations], ed. J. Jacob and P. Marchand. Trans. R. Kneipp. Paris: Association Française de Génie Civil.

Banthia, N. 2005. Impact resistance of HPFRCC. In *International workshop on high performance fiber reinforced cementitious composites in structural applications, 23-26 May, Honolulu, HI*, ed. G. Fischer and V. C. Li, 479–488. Bagneux, France: RILEM.

Bauchau, O. A., and J. I. Craig. 2009. *Structural analysis with applications to aerospace structures*. Dordrecht, Netherlands: Springer.

Bierwagen, D., and A. Abu-Hawash. 2005. Ultra high performance concrete highway bridge. In *Mid-Continent Transportation Research Symposium, 18-19 August, Ames, IA*. Ames, IA: University of Iowa.

Blais, P. Y., and M. Couture. 1999. Precast, prestressed pedestrian bridge-world's first reactive powder concrete structure. *PCI Journal* 44:60–71.

Brühwiler, E., and E. Denarié. 2008. Rehabilitation of concrete structures using ultra-high performance fibre reinforced concrete. In *The Second International Symposium on Ultra-High Performance Concrete, 5-7 March, Kassel, Germany*, ed. E. Fehling, M. Schmidt and S. Stürwald. Kassel, Germany: Kassel University Press.

Buchholdt, H. A. 1997. *Structural dynamics for engineers*. London: Thomas Telford.

Budynas, R. G. 1999. *Advanced strength and applied stress analysis*. 2nd ed. Boston: McGraw-Hill.

Buitelaar, P., R. Braam, and N. Kaptijn. 2004. Reinforced high performance concrete overlay system for rehabilitation and strengthening of orthotropic steel bridge decks. In *Orthotropic Bridge Conference, 23-27 August, Sacramento, CA*. 384–401.

Cadoni, E., C. Albertini, and G. Solomos. 2006. Analysis of the concrete behaviour in tension at high strain-rate by a modified Hopkinson bar in support of impact resistant structural design. *Journal De Physique IV* 134:647–652.

Cavill, B., M. Rebentrost, and V. Perry. 2006. Ductal®-an ultra-high performance material for resistance to blasts and impacts. In *1st Specialty Conference on Disaster Mitigation, 23–26 May, Calgary*. Alberta, Canada.

CEB-FIP. 1993. *Design of concrete structures*. CEB FIP model code 1990. London: British Standard Institution.

Colombo, M., and P. Martinelli. 2011. SDOF models for RC and FRC circular plates under blast loads. *Applied Mechanics and Materials* 82:440–445.

Del Viso, J., J. Carmona, and G. Ruiz. 2008. Shape and size effects on the compressive strength of high-strength concrete. *Cement and Concrete Research* 38(3):386–395.

Denarié, E., E. Brühwiler, A. Znidaric, Y. Houst, and R. Rohleder. 2005. *Full scale application of UHPFRC for the rehabilitation of bridges – from the lab to the field*. Sustainable and Advanced MAterials for Road InfraStructure (SAMARIS) WP 14: HPFRCC Report D22. Roskilde, Denmark: SAMARIS Secretariat, Danish Road Institute.

Densit ApS. a. *Data sheet: Ducorit® - ultra high performance grout*.

–––. b. *Data sheet: FLEXBINDER - a castable material*.

–––. c. *Data sheet: INDUCAST TT-5 - a castable material*.

Douglas, K. S., and S. L. Billington. 2005. Rate dependence in high-performance fiber-reinforced cement-based composites for seismic applications. In *International workshop on high performance fiber reinforced cementitious composites in structural applications, 23–26 May, Honolulu, HI,* ed. G. Fischer and V. C. Li, 17–25. Bagneux, France: RILEM.

Ellis, B. D., B. P. DiPaolo, D. L. McDowell, and M. Zhou. 2014. Experimental investigation and multiscale modeling of ultra-high-performance concrete panels subject to blast loading. *International Journal of Impact Engineering* 69:95–103.

Fehling, E., M. Schmidt, T. Teichmann, K. Bunje, R. Bornemann, and B. Middendorf. 2005. *Entwicklung, dauerhaftigkeit und berechnung ultrahochfester betone (UHPC): Forschungsbericht DFG FE 497/1-1*. Kassel, Germany: Kassel University Press.

Foust, B. W., and T. S. Oesch. 2012. *Parametric study of innovative materials used for blast mitigation*. ERDC/GSL TR-12-22. Vicksburg, MS: US Army Engineer Research and Development Center. DTIC accession number ADB392165.

Fujikake, K., T. Senga, N. Ueda, T. Ohno, and M. Katagiri. 2006. Study on impact response of reactive powder concrete beam and its analytical model. *Journal of Advanced Concrete Technology* 4(1):99–108.

Fujikura, S., M. Bruneau, and D. Lopez-Garcia. 2008. Experimental investigation of multihazard resistant bridge piers having concrete-filled steel tube under blast loading. *Journal of Bridge Engineering* 13(6):586–594.

Graybeal, B. A. 2006. *Material property characterization of ultra-high performance concrete*. FHWA-HRT-06-103. McLean, VA: Federal Highway Administration.

Graybeal, B., and M. Davis. 2008. Cylinder or cube: Strength testing of 80 to 200 MPa (11.6 to 29 ksi) ultra-high-performance fiber-reinforced concrete. *ACI Materials Journal* 105(6):603–609.

Habel, K., and P. Gauvreau. 2008. Response of ultra-high performance fiber reinforced concrete (UHPFRC) to impact and static loading. *Cement and Concrete Composites* 30(10):938–946.

Harris, D. K., J. Sarkar, and T. M. Ahlborn. 2011. Characterization of interface bond of ultra-high-performance concrete bridge deck overlays. *Transportation Research Record: Journal of the Transportation Research Board* 2240:40–49.

Jacquelin, E., and P. Hamelin. 2001. Block-bar device for energy absorption analysis. *Mechanical Systems and Signal Processing* 15(3):603-617.

Karihaloo, B. 2012. CARDIFRC–From concept to industrial application. In *High Performance Fiber Reinforced Cement Composites 6, 19-22 June 2011, Ann Arbor, MI*, ed. G. J. Parra-Montesinos, H. W. Reinhardt and A. E. Naaman, 397–404. Berlin: Springer.

Keierleber, B., B. Phares, D. Bierwagen, I. Couture, and F. Fanous. 2007. Design of Buchanan County, Iowa, bridge using ultra high performance concrete and PI girders. In *The 2007 Mid-Continent Transportation Research Symposium, 16–17 August, Ames, IA.*. Ames, IA: Iowa State University.

Kelly, P. A. 2013. *Lecture notes in solid mechanics part II: Engineering solid mechanics.* Auckland, New Zealand: Department of Engineering Science, University of Auckland.

Kiger, S. A., H. A. Salim, and A. Ibrahim. 2010. *Bridge vulnerability assessment and mitigation against explosions*. MTC Project 2007-06. Ames, IA: Midwest Transportation Consortium.

Lafarge. Products & technical specifications. 2014. http://www.ductal-lafarge.com/wps/portal/ductal/6_2-Products_and_technical_datasheet.

Lafarge Canada Inc. 2009a. *Product data sheet: Ductal BS1000*. Ontario: Lafarge Canada.

———. 2009b. *Product data sheet: Ductal CS1000*. Ontario: Lafarge Canada.

Lai, J., and W. Sun. 2008. Dynamic mechanical behaviour of ultra-high performance fiber reinforced concretes. *Journal of Wuhan University of Technology-Materials Science Edition* 23(6):938–945.

———. 2009. Dynamic behaviour and visco-elastic damage model of ultra-high performance cementitious composite. *Cement and Concrete Research* 39(11):1044–1051.

———. 2010. Dynamic damage and stress-strain relations of ultra-high performance cementitious composites subjected to repeated impact. *Science China Technological Sciences* 53(6):1520–1525.

Lemaitre, J., and J. Chaboche. 1990. *Mechanics of solid materials*. Cambridge: Cambridge University Press.

Li, V. C. 2003. On engineered cementitious composites (ECC). *Journal of Advanced Concrete Technology* 1(3):215–230.

Li, V. C., S. Wang, and C. Wu. 2001. Tensile strain-hardening behavior of polyvinyl alcohol engineered cementitious composite (PVA-ECC). *ACI Materials Journal* 98(6):483–492.

Maalej, M., S. Quek, and J. Zhang. 2005. Behavior of hybrid-fiber engineered cementitious composites subjected to dynamic tensile loading and projectile impact. *Journal of Materials in Civil Engineering* 17(2):143–152.

Malvar, L. J., and C. A. Ross. 1998. Review of strain rate effects for concrete in tension. *ACI Materials Journal* 95(6):735–739.

Mansur, M., and M. Islam. 2002. Interpretation of concrete strength for nonstandard specimens. *Journal of Materials in Civil Engineering* 14(2):151–155.

Mechtcherine, V., O. Millon, M. Butler, and K. Thoma. 2012. Mechanical behavior of SHCC under impact loading. In *High Performance Fiber Reinforced Cement Composites 6, 19-22 June 2011, Ann Arbor, MI,* ed. G. J. Parra-Montesinos, H. W. Reinhardt and A. E. Naaman, 297–304. Berlin: Springer.

Mechtcherine, V., F. d. A. Silva, M. Butler, D. Zhu, B. Mobasher, S. Gao, and E. Mäder. 2011. Behaviour of strain-hardening cement-based composites under high strain rates. *Journal of Advanced Concrete Technology* 9(1):51–62.

Mehta, P. K., and P. J. Monteiro. 2006. *Concrete: Microstructure, properties, and materials*. 3rd ed. New York: McGraw-Hill.

Millard, S. G., T. C. K. Molyneaux, S. J. Barnett, and X. Gao. 2010. Dynamic enhancement of blast-resistant ultra high performance fibre-reinforced concrete under flexural and shear loading. *International Journal of Impact Engineering* 37(4):405–413.

Millon, O., W. Riedel, K. Thoma, E. Fehling, and M. Nöldgen. 2009. Fiber-reinforced ultra-high performance concrete under tensile loads. In *DYMAT 2009 - 9th International Conference on the Mechanical and Physical Behaviour of Materials under Dynamic Loading, 7-11 September, Brussels*, 1:671–677. Les Ulis, France: EDP Sciences.

Neville, A. M. 1966. A general relation for strengths of concrete specimens of different shapes and sizes. *Journal of the American Concrete Institute* 63(10):1095–1109.

Newmark, N. M. 1953. An engineering approach to blast resistant design. In *Proceedings, American Society of Civil Engineers Convention*, *19-22 October, New York City*, 79(306):1–16. New York: ASCE.

Ngo, T., and P. Mendis. 2008. Modelling reinforced concrete structures subjected to impulsive loading using concrete lattice model. *Electronic Journal of Structural Engineering* 8:80–89.

Ngo, T., P. Mendis, A. Gupta, and J. Ramsay. 2007a. Blast loading and blast effects on structures–an overview. *Electronic Journal of Structural Engineering* 7:76–91.

Ngo, T., P. Mendis, and T. Krauthammer. 2007b. Behavior of ultrahigh-strength prestressed concrete panels subjected to blast loading. *Journal of Structural Engineering* 133(11):1582–1590.

Nöldgen, M., W. Riedel, K. Thoma, and E. Fehling. 2013. Properties of ultra high performance concrete (UHPC) in tension at high strain rates. In *VIII International Conference on Fracture Mechanics of Concrete and Concrete Structures, 10–14 March, Toledo, Spain*, ed. J. G. M. van Mier, G. Ruiz, C. Andrade, R. C. Yu and X. X. Zhang. University of Castilla La-Mancha.

Oñate, E. 2013. Thin plates: Kirchhoff theory. In *Structural analysis with the finite element method. Linear statics*. Vol. 2, 233-290. Barcelona, Spain: Springer Netherlands jointly with International Center for Numerical Methods in Engineering.

Parant, E., P. Rossi, E. Jacquelin, and C. Boulay. 2007. Strain rate effect on bending behavior of new ultra-high-performance cement-based composite. *ACI Materials Journal* 104(5):458–463.

Park, S. H., D. J. Kim, G. S. Ryu, and K. T. Koh. 2012. Tensile behavior of ultra high performance hybrid fiber reinforced concrete. *Cement and Concrete Composites* 34(2):172–184.

Raphael, J. M. 1984. Tensile strength of concrete. *ACI Journal* 81(2):158–165.

Rebentrost, M., and G. Wight. 2011. Investigation of UHPFRC slabs under blast loads. In *Designing and Building with Ultra-High Performance Fibre-Reinforced Concrete (UHPFRC): State of the Art and Development, 17–18 November 2009, Marseille, France*, ed. F. Toulemonde and J. Resplendino, 189–208. Hoboken, NJ: Wiley-ISTE.

Richard, P., and M. Cheyrezy. 1995. Composition of reactive powder concretes. *Cement and Concrete Research* 25(7):1501–1511.

Rong, Z., W. Sun, and Y. Zhang. 2010. Dynamic compression behavior of ultra-high performance cement based composites. *International Journal of Impact Engineering* 37(5):515–520.

Rossi, P., A. Arca, E. Parant, and P. Fakhri. 2005. Bending and compressive behaviours of a new cement composite. *Cement and Concrete Research* 35(1):27–33.

Rossi, P., and E. Parant. 2008. Damage mechanisms analysis of a multi-scale fibre reinforced cement-based composite subjected to impact and fatigue loading conditions. *Cement and Concrete Research* 38(3):413–421.

Schuler, H. 2004. Experimentelle und numerische untersuchungen zur schädigung von stoßbeanspruchtem beton. epsilon–Forschungsergebnisse aus der kurzzeitdynamik, heft 6. PhD diss., Fraunhofer Institut für Kurzzeitdynamik, EMI.

Schuler, H., and H. Hansson. 2006. Fracture behaviour of high performance concrete (HPC) investigated with a Hopkinson-bar. *Journal De Physique IV* 134:1145–1151.

Schuler, H., C. Mayrhofer, and K. Thoma. 2006. Spall experiments for the measurement of the tensile strength and fracture energy of concrete at high strain rates. *International Journal of Impact Engineering* 32(10):1635–1650.

Shaheen, E., and N. G. Shrive. 2007. Cyclic loading and fracture mechanics of Ductal® concrete. *International Journal of Fracture* 148(3):251–260.

Silva, F. d. A., D. Zhu, B. Mobasher, C. Soranakom, and R. D. Toledo Filho. 2010. High speed tensile behavior of sisal fiber cement composites. *Materials Science and Engineering: A* 527(3):544–552.

Solomos, G., and M. Berra. 2004. *Testing of anchorages in concrete under dynamic loading*. EUR 21094 EN. Ispra, Italy: European Commission.

Thoma, K., A. Stolz, and O. Millon. 2012. Performance and suitability of ultra-high-performance concrete under a broad range of dynamic loadings. In *Advances in Protective Structures Research, 29 September–1 October 2010, Manchester, UK*, ed. H. Hao and Z. Li, 1:65–96. Boca Raton, FL: CRC Press.

Ulfkjær, J., K. Labibes, G. Solomos, and C. Albertini. 1998. Tensile failure of normal concrete and steel fiber reinforced concrete at high strain rates. In *Fracture Mechanics of Concrete Structures 3, 12–16 October, Gifu, Japan*, ed. H. Mihashi and K. Rokugo, 1:585–597. Freiburg, Germany: AEDIFICATIO.

USACE (US Army Corps of Engineers), Naval Facilities Engineering Command, and Air Force Civil Engineer Support Agency. 2008. *Structures to resist the effects of accidental explosions*. UFC 3-340-02. Washington, DC: US Department of Defense.

Walker, R. E., J. C. Ray, L. A. Walker, and J. K. Minor. 2011. *Validation of numerical modeling and analysis of steel bridge towers subjected to blast loadings: Series 3 report*. ERDC/GSL TR-11-11. Vicksburg, MS: US Army Engineer Research and Development Center.

Wang, L. 2007. *Foundations of stress waves*. Amsterdam: Elsevier.

Wang, L., D. Huang, and S. Gan. 1996. Nonlinear viscoelastic constitutive relations and nonlinear viscoelastic wave propagation for polymers at high strain rates. In *Constitutive relation in High/Very high strain rates,* 137–146. Berlin: Springer.

Wang, S., and V. Li. 2003. Lightweight engineered cementitious composites (ECC). In *RILEM International Workshop, High Performance Fiber Reinforced Cement Composites, 16-18 June, Ann Arbor, MI,* ed. A. Naaman and H. Reinhardt, 379–390. Bagneux, France: RILEM.

Webster, J. L., P. E. Reicher, and G. L. Cohen. 2006. *Antiterrorism measures for historic properties*. ERDC/CERL TR-06-23. Champaign, IL: US Army Engineer Research and Development Center.

Weckert, S., T. Weerasooriya, and C. A. Gunnarson. 2011. Loading rate effect on the tensile failure of concrete and its constituents using diametrical compression and direct tension. In *Dynamic behavior of materials.*, ed. T. Proulx, Vol. 1, 13–27. New York: Springer.

Williams, E. M., S. S. Graham, P. A. Reed, and T. S. Rushing. 2009. *Laboratory characterization of Cor-Tuf concrete with and without steel fibers.* ERDC/GSL TR-09-22. Vicksburg, MS: US Army Engineer Research and Development Center.

Williamson, E. B., O. Bayrak, G. D. Williams, C. E. Davis, K. A. Marchand, A. E. McKay, J. Kulicki, and W. Wassef. 2010. *Blast-resistant highway bridges: Design and detailing guidelines.* NCHRP 645. Washington, DC: Transportation Research Board.

Winget, D. G., K. A. Marchand, and E. B. Williamson. 2005. Analysis and design of critical bridges subjected to blast loads. *Journal of Structural Engineering* 131(8):1243–1255.

Yang, E., and V. C. Li. 2005. Rate dependence in engineered cementitious composites. In *International workshop on high performance fiber reinforced cementitious composites in structural applications, 23–26 May, Honolulu, HI*, ed. G. Fischer and V. C. Li, 83–92. Bagneux, France: RILEM.

Yi, S., E. Yang, and J. Choi. 2006. Effect of specimen sizes, specimen shapes, and placement directions on compressive strength of concrete. *Nuclear Engineering and Design* 236(2):115–127.

Zdeb, T. 2013. Ultra-high performance concrete–properties and technology. *Bulletin of the Polish Academy of Sciences: Technical Sciences* 61(1):183–193.

Appendix A: Dynamic Property Calculation

B5Q tensile strength

Because the dynamic tensile strength data for B5Q in Section 3.3.1 are at strain rates above 100 s⁻¹, the modified CEB-FIP model from Malvar and Ross (1998) was used to calculate the dynamic strength at 20 s⁻¹. This model was found by Nöldgen et al. (2013) to fit their data for B5Q well. In the equations below, f_{td} and f_{ts} are the dynamic and static tensile strengths, respectively (MPa); $\dot{\varepsilon}$ is the strain rate; $\dot{\varepsilon}_s$ is the quasi-static strain rate, $\dot{\varepsilon}_s = 10^{-6}$ s⁻⁶; f'_{cs} is the static compressive strength (MPa); and δ and β are dimensionless fitting parameters. The dynamic tensile strength was calculated as:

$$\delta = \frac{1}{1 + \frac{8f'_{cs}}{10\text{ MPa}}} = \frac{1}{1 + \frac{8(208\text{ MPa})}{10\text{ MPa}}} = 0.005974$$

$$\beta = 10^{6\delta - 2} = 10^{6(0.005974) - 2} = 0.010860$$

$$f_{td} = f_{ts}\,\beta \left(\frac{\dot{\varepsilon}}{\dot{\varepsilon}_s}\right)^{\frac{1}{3}} = (10.5\text{ MPa})(0.010860)\left(\frac{20\text{ s}^{-1}}{10^{-6}\text{ s}^{-6}}\right)^{\frac{1}{3}}$$

$$f_{td} = 31.0\text{ MPa} = 4490\text{ psi}$$

CEMTEC$_{\text{multiscale}}$® tensile strength

The tensile strength σ_{UTS} for CEMTEC$_{\text{multiscale}}$® was converted from the modulus of rupture σ_{MOR} using the approximate linear correlation $\sigma_{UTS} = 0.60651\sigma_{MOR} - 2.4899$, with coefficient of determination $r^2 = 0.9279$ and all values in ksi. The highest strain rate with experimental data was 13.2 s⁻¹, so the measured value of $\sigma_{MOR} = 35.4$ ksi at that rate was used. The dynamic tensile strength is then approximately $\sigma_{UTS} = 0.60651(35.4) - 2.4899 = 19$ ksi $= 19000$ psi.

Ductal® compressive strength

The dynamic compressive strength of Ductal® at a strain rate of 20 s⁻¹ was calculated using the model proposed by Ngo and others (Ngo and Mendis 2008; Ngo 2007b):

$$f'_{cd} = f'_{cs}\left(\frac{\dot{\varepsilon}}{\dot{\varepsilon}_s}\right)^{1.026\alpha} \qquad \text{for } \dot{\varepsilon} \leq \dot{\varepsilon}_1 \text{ and}$$

$$f'_{cd} = f'_{cs}(A_1 \ln(\dot{\varepsilon}) - A_2) \text{ for } \dot{\varepsilon} > \dot{\varepsilon}_1,$$

where f'_{cd} is the dynamic peak stress (MPa); f'_{cs} is the static compressive strength (MPa); $\dot{\varepsilon}$ is the strain rate (s⁻¹); $\dot{\varepsilon}_s$ is the quasi-static strain rate, $\dot{\varepsilon}_s = 3 \times 10^{-5}$ s⁻¹; α, A_1, and A_2 are fitting parameters, and $\dot{\varepsilon}_1$ is the turning-point strain rate (s⁻¹). For Ductal® at $\dot{\varepsilon} = 20$ s⁻¹,

$$\alpha = \frac{1}{20 + \frac{f'_{cs}}{2}} = \frac{1}{20 + \frac{160 \text{ MPa}}{2}} = 0.01 \ and$$

$$\dot{\varepsilon}_1 = 0.0022(f'_{cs})^2 - 0.1989 f'_{cs} + 46.137$$
$$= 0.0022(160 \text{ MPa})^2 - 0.1989(160 \text{ MPa}) + 46.137 = 70.633 \text{ s}^{-1}.$$

Since $20 \text{ s}^{-1} < \dot{\varepsilon}_1$, the dynamic tensile strength is

$$f'_{cd} = f'_{cs}\left(\frac{\dot{\varepsilon}}{\dot{\varepsilon}_s}\right)^{1.026\alpha} = (160 \text{ MPa})\left(\frac{20 \text{ s}^{-1}}{3 \times 10^{-5} \text{ s}^{-1}}\right)^{1.026(0.01)} = 184 \text{ MPa}$$
$$= 26600 \text{ psi}.$$

B5Q, CEMTEC~multiscale~®, and SHCC/ECC compressive strength DIFs

In the absence of dynamic compressive strength data for these three materials, a DIF of 1.1 was applied to their static compressive strengths to obtain an approximate estimate of their dynamic performance. The DIF is based on the performance of the other materials at this strain rate, which had DIFs around 1.2, but was conservatively lowered to 1.1, since little is actually known about these materials' dynamic compressive behavior. The choice of DIF is approximately 1.16 suggested by UFC 3-340-02 (USACE 2008) for conventional concrete in compression from close-in blast loading. It is known that UHPC, with a higher static compressive strength, generally exhibits a weaker rate-dependence than conventional concrete.

Sample calculations using the DIF are shown in Table A1, with static values taken from Section 4.2.

Table A-1. DIF example calculations.

Material	Static Compressive Strength (psi)	Dynamic Compressive Strength (psi)
B5Q	30200	1.1 × 30200 = 33200
CEMTEC~multiscale~®	29700	1.1 × 29700 = 32700
SHCC/ECC	8800	1.1 × 8800 = 9700

Appendix B: Model Results

Table B-1. Compiled SDOF results.

Simulation ID	Maximum Deflection, x_m (in.)	Time of Occurrence (µs)	Ductility Ratio, μ (−)	Relative Deflection, x_m/L (−)	Support Rotation, θ (deg)
D-1-P	0.0390	755	2.111	0.001	0.112
D-1-A	0.0390	760	2.111	0.001	0.112
D-2-P	0.1514	1250	8.197	0.004	0.434
D-2-A	0.1514	1250	8.197	0.004	0.434
D-3a-P	0.7816	2715	42.316	0.020	2.238
D-3a-A	0.7816	2715	42.316	0.020	2.238
D-3b-P	1.6560	3925	89.656	0.041	4.733
D-3b-A	1.6560	3925	89.656	0.041	4.733
F-1-P	0.0397	895	3.439	0.001	0.114
F-1-A	0.0397	895	3.439	0.001	0.114
F-2-P	0.1690	1570	14.640	0.004	0.484
F-2-A	0.1690	1570	14.640	0.004	0.484
F-3a-P	0.8936	3485	77.410	0.022	2.558
F-3a-A	0.8937	3485	77.418	0.022	2.559
F-3b-P	1.8998	5055	164.574	0.047	5.426
F-3b-A	1.8998	5055	164.574	0.047	5.426
B-1-P	0.0324	655	1.559	0.001	0.093
B-1-A	0.0324	655	1.559	0.001	0.093
B-2-P	0.1158	1010	5.572	0.003	0.332
B-2-A	0.1158	1010	5.572	0.003	0.332
B-3a-P	0.5834	2145	28.072	0.015	1.671
B-3a-A	0.5834	2145	28.072	0.015	1.671
B-3b-P	1.2317	3090	59.267	0.031	3.524
B-3b-A	1.2318	3095	59.272	0.031	3.524
C-1-P	0.0310	655	0.293	0.001	0.089
C-1-A	0.0310	655	0.293	0.001	0.089
C-2-P	0.0675	590	0.638	0.002	0.193
C-2-A	0.0675	590	0.638	0.002	0.193
C-3a-P	0.1689	660	1.597	0.004	0.484

Simulation ID	Maximum Deflection, x_m (in.)	Time of Occurrence (µs)	Ductility Ratio, μ (–)	Relative Deflection, x_m/L (–)	Support Rotation, Θ (deg)
C-3a-A	0.1689	665	1.597	0.004	0.484
C-3b-P	0.2983	845	2.821	0.007	0.855
C-3b-A	0.2983	850	2.821	0.007	0.855
S-1-P	0.0948	1340	3.987	0.002	0.272
S-1-A	0.0918	1345	3.861	0.002	0.263
S-2-P	0.3918	2410	16.478	0.010	1.122
S-2-A	0.3918	2415	16.478	0.010	1.122
S-3a-P	2.0555	5400	86.448	0.051	5.868
S-3a-A	2.0555	5400	86.448	0.051	5.868
S-3b-P	4.3643	7840	183.550	0.109	12.310
S-3b-A	4.3643	7845	183.550	0.109	12.310

REPORT DOCUMENTATION PAGE

1. REPORT DATE *(DD-MM-YYYY)*	2. REPORT TYPE	3. DATES COVERED *(From - To)*
April 2023	Final	

4. TITLE AND SUBTITLE

Advanced Cementitious Materials for Blast Protection

5a. CONTRACT NUMBER

5b. GRANT NUMBER

5c. PROGRAM ELEMENT NUMBER

6. AUTHOR(S)

Andrew B. Groeneveld and C. Kennan Crane

5d. PROJECT NUMBER

5e. TASK NUMBER

5f. WORK UNIT NUMBER

7. PERFORMING ORGANIZATION NAME(S) AND ADDRESS(ES)

Geotechnical and Structures Laboratory
US Army Engineer Research and Development Center
3909 Halls Ferry Road
Vicksburg, MS 39180-6199

8. PERFORMING ORGANIZATION REPORT NUMBER

ERDC/GSL TR-23-6

9. SPONSORING / MONITORING AGENCY NAME(S) AND ADDRESS(ES)

Federal Highway Administration
Turner-Fairbank Highway Research Center
McLean, VA 22101

10. SPONSOR/MONITOR'S ACRONYM(S)

11. SPONSOR/MONITOR'S REPORT NUMBER(S)

12. DISTRIBUTION / AVAILABILITY STATEMENT
DISTRIBUTION STATEMENT A. Approved for public release: distribution is unlimited.

13. SUPPLEMENTARY NOTES
Material Specifications for Attack Countermeasures on Bridges; IAA DTFH61-10-X-30028 and IAA DTFH61-13-X-30049

14. ABSTRACT

Advanced cementitious materials, commonly referred to as ultra-high performance concretes (UHPCs), are developing rapidly and show promise for civil infrastructure and protective construction applications. Structures exposed to blasts experience strain rates on the order of 10^2 s^{-1} or more. While a great deal of research has been published on the durability and the static properties of UHPC, there is less information on its dynamic properties. The purpose of this report is to (1) compile existing dynamic property data–including compressive strength, tensile strength, elastic modulus, and energy absorption–for six proprietary and research UHPCs and (2) implement a single-degree-of-freedom (SDOF) model for axisymmetric UHPC panels under blast loading as a means of comparing the UHPCs. Although simplified, the model allows identification of key material properties and promising materials for physical testing. Model results indicate that tensile strength has the greatest effect on panel deflection, with unit weight and elastic modulus having a moderate effect. CEMTEC$_{\text{multiscale}}$® deflected least in the simulation. Lafarge Ductal®, a commonly available UHPC in North America, performed in the middle of the five UHPCs considered.

15. SUBJECT TERMS

Ultra-high performance concrete (UHPC)	Dynamic mechanical property	Single-degree-of-freedom (SDOF) model
Dynamic compressive strength	Dynamic tensile strength	Bridges
Explosions	Protective construction	Blast effect
	Cement composites–Dynamic testing	High strength concrete–Dynamic testing

16. SECURITY CLASSIFICATION OF:

a. REPORT	b. ABSTRACT	c. THIS PAGE	17. LIMITATION OF ABSTRACT	18. NUMBER OF PAGES	19a. NAME OF RESPONSIBLE PERSON
Unclassified	Unclassified	Unclassified	SAR	85	19b. TELEPHONE NUMBER *(include area code)*